Generating optimal Gravitational-Wave template banks with metric-preserving autoencoders

Giovanni Cabass, 1, * Digvijay Wadekar, 2, 3 Matias Zaldarriaga, 4 and Zihan Zhou⁵

¹Division of Theoretical Physics, Ruder Bošković Institute, Zagreb HR-10000, Croatia

We present a geometric placement algorithm for constructing template banks. We specialize in the case of Gravitational Wave searches, and use autoencoders for non-linear compression of the space of waveforms after these have been represented by a finite number of basis functions using an SVD decomposition. To ensure that the autoencoder is suitable for geometric placement we try to find a coordinate system describing the manifold of SVD coefficients such that distances in the latent and embedding space are equal. We show that the curvature of the banks is negligible and that such a system can be found. We then show that a geometric placement algorithm via a uniform grid in the latent space combined with rejection of unphysical points using a normalizing flow results in templates that, while slightly less in number than the similar construction using random forests of Ref. [1], perform slightly better in the effectualness tests, especially for high-mass binary systems. We discuss briefly how these dimensionality reduction techniques might be used in the context of cosmology, and a simple toy example where the periodicity of a flat manifold slightly complicates finding a distance-preserving coordinate system.

1. INTRODUCTION

Template banks are systematically-constructed collections of "template" waveforms or patterns used to identify or extract signals embedded in noisy data by matched filtering (comparing the data to each template). Template banks are crucial in signal-detection any field where: (i) the expected signal shape is parameterizable, (ii) the data is noisy, (iii) direct identification is challenging. Template banks have been used in various areas of physics and astronomy, such as Gravitational Wave (GW) Astronomy (the main topic of this paper, see e.g. [2–17] as references), Pulsar and Fast Radio Burst (FRB) Searches, Exoplanet Transit and Radial Velocity Searches, Binary Star/Compact Object Searches in X-ray and Gamma-ray Astronomy, Signal Processing in Particle Physics, Cosmic Ray and Air Shower Detection, among many more.

Typically, the signal waveforms are high-dimensional but most of variation in the waveforms is along only a few effective dimensions. For example, in GW waveforms, the most variation occurs along the dimension of the binary chirp mass. The dimensionality of the template bank is set by these effective dimensions. Thus the problem becomes to capture the variation in signal waveforms into the minimum possible number of dimensions while also retaining accuracy. Apart from being of the right dimensions, the banks should have templates optimally spaced along the dimensions, otherwise this introduces redundancies (as overly-close templates give the same result) and this also increases the search computational cost. This goes under the name of geometric placement, see e.g. [18]. Machine Learning architectures like autoencoders are good at dimensionality reduction but do not typically preserve the metric in the input space. We therefore construct metric-preserving autoencoders in this paper using a hybrid loss function given by $L = \alpha \times L_{\text{reconstruction}} + \beta \times L_{\text{distance preservation}}$, where α and β are hyperparameters. Autoencoders are

²Department of Physics and Astronomy, Johns Hopkins University, 3400 N. Charles Street, Baltimore, Maryland, 21218, USA

³ Weinberg Institute, University of Texas at Austin, Austin, TX 78712, USA

School of Natural Sciences, Institute for Advanced Study, 1 Einstein Drive, Princeton, NJ 08540, USA
 Department of Physics, Princeton University, Princeton, NJ 08540, USA

^{*} giovanni.cabass@gmail.com

neural network architectures which have a latent bottleneck layer with lower-dimensionality than the input. The input data is therefore compressed into a latent vector and then transformed back to the original dimensions $c \to d \to \hat{c}$. The reconstruction loss is based on the difference between c and \hat{c} . We will use the metric preservation loss to enforce $|c-c'| \approx |d-d'|$.

Crucially, this requires a concept of distance in the embedding space. This distance was identified in Ref. [18]. In this work, the space of templates was first subdivided in banks by isolating waveforms $h(\mathbf{p}, f) = A(\mathbf{p}, f) \exp i\Psi(\mathbf{p}, f)$ – \mathbf{p} being the binary's parameters and f the frequency – that have a similar amplitude profile and placing them in 17 banks BBH-0 to BBH-16, and then further subdividing these banks in sub-banks based on the chirp mass \mathcal{M} , that controls the duration of the signal. Then, one performs a dimensionality reduction for the phases using SVD, in such a way that $\Psi(\mathbf{p}, f)$ in each sub-bank can be described by a finite (and small) number of basis functions and respective SVD coefficients (the 22 subscript below indicating the fact that we focus on the leading quadrupole mode):

$$\Psi_{22}(\boldsymbol{p}, f) = \langle \Psi_{22} \rangle_{\text{sub-bank}}(f) + \sum_{A=0}^{\text{few}} c^A(\boldsymbol{p}) \Psi_A^{\text{SVD}}(f) , \qquad (1)$$

where $\langle \cdot \rangle_{\text{sub-bank}}$ denotes that we construct the SVD after subtracting the average over all the examples in a given sub-bank, and "few" will be equal to 9 in the remainder of this paper. Then, the search proceeds by performing geometric placement of the templates in the much more manageable space of the SVD coefficients c^A . More precisely, the construction of the template bank involves creating a uniform grid in the space of the SVD coefficients, inspired by the fact that the mismatch between templates in a given sub-bank is well approximated by the Euclidean distance between the c^A :

$$\langle h(c)|h(c+\delta c)\rangle \approx 1 - \frac{\delta_{AB}c^Ac^B}{2}$$
 (2)

We then see that the distance we will want to preserve in the latent space of our autoencoder is the Euclidean distance in the space of the SVD coefficients c^A . Guidance on the dimension of the latent space comes from Ref. [1]. This work performed a further dimensionality reduction after the SVD decomposition: it was observed that the c^A lie on a 2-dimensional sub-manifold of \mathbb{R}^{10} , which Ref. [1] described using random forests. Hence, in this work we will autoencode the sub-manifold where the c^A lie $-c \xrightarrow{\mathcal{E}} e \xrightarrow{\mathcal{D}} c$ – and ensure both that close points in the latent space correspond to close points in the embedding space and that a uniform grid of equally-spaced (e^0, e^1) corresponds to equally-distant (e^0, e^1) . In other words, we want to find "coordinates" e^{μ} such that the metric is flat. This is not needed if we describe the sub-manifolds using random forests as in [1], and presents an additional challenge if one wants to use autoencoders for dimensionality reduction.

The main result of the paper are Figs. 2 and 3 (that summarize the effectualness of our template banks), together with Tab. I (which shows the number of templates per bank and sub-bank). We compare our results using autoencoders to those of Ref. [1], showing that the template banks constructed with autoencoders perform slightly better than the ones constructed with random forests while containing a slightly smaller number of templates across all banks and sub-banks. Most importantly, however, we emphasize the difference between linear and non-linear dimensionality reduction techniques by comparing our results to what one would obtain by taking only the first 2 SVD coefficients to construct the waveforms.

2. TEMPLATE BANKS FOR GRAVITATIONAL WAVE SEARCHES

We first review the case – already studied in Ref. [1] – of using random forests to model the leading SVD coefficients $(c^0, c^1, \ldots c^9)$ for the phase profile of the templates in each amplitude bank and chirp mass sub-bank, comparing it to the case where we consider only the first 2 SVD coefficients (c^0, c^1) and put to 0 the others. Then we move to using autoencoders to model $(c^0, c^1, \ldots c^9)$.

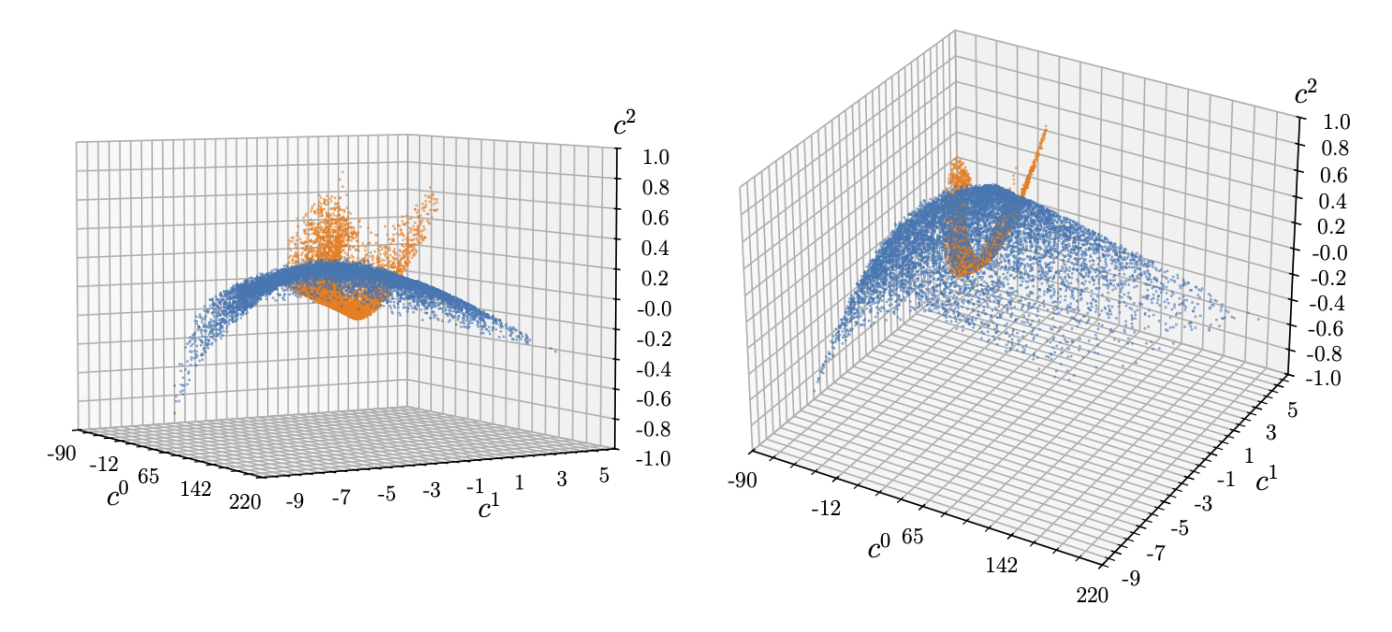


FIG. 1: The first three components of the SVD coefficients c^A for Bank 0 (teal) and Bank 4 (orange).

Our template banks are listed in Tab. I. Our plots focus on three banks, two at the high-mass and one at the low-mass end: BBH-0, $\mathcal{M} \in [2.6, 5.3] \, M_{\odot}$, BBH-4, $\mathcal{M} \in [5.8, 10.8] \, M_{\odot}$ and BBH-12, $\mathcal{M} \in [28.4, 173.5] \, M_{\odot}$. In the remainder of the text and of the figures, we will denote these by "Bank 0", "Bank 4", "Bank 12" for simplicity. We show the first three SVD components for Bank 0 and Bank 4 in Fig. 1. We see that the manifold of the c^A is very "curved", in the sense that it is easy to see by eye that it is not a manifold described by a system of inhomogeneous linear equations. Hence we expect that nonlinear dimensionality reduction methods will perform much better than linear ones in reproducing the template waveforms.

2.1. Dimensionality reduction with random forests

As discussed in Section 1, in the case of the random forest our templates are constructed by first generating many examples for the phases in each bank and sub-bank, constructing the SVD decomposition as in [18], and then fitting a random forest RF (we use https://scikit-learn.org/stable/modules/generated/sklearn.ensemble. RandomForestRegressor.html, with 50 trees and maximum depth of 50) to predict $(c^2, c^3, \dots c^9) = RF(c^0, c^1)$ [1]. In the upper-right panel of Fig. 2 we show the phase reconstruction error in the validation dataset

phase overlap =
$$\left| \left\langle A_{22}^{\text{sub-bank}} e^{i\Psi_{22}} \middle| A_{22}^{\text{sub-bank}} e^{i\Psi_{22}^{\text{model}}} \right\rangle \right|$$
 (3)

for the training of this random forest. We can compare this with the upper-left panel of that figure, where instead we take consider only the first two SVD coefficients (c^0, c^1) and we put $(c^2, c^3, \dots c^9)$ to zero.

Let us then move to the construction of the template banks themselves.¹ As in Ref. [1], we adapt the geometric placement method of [18] to the case where $(c^2, c^3, \dots c^9) = \text{RF}(c^0, c^1)$. This is straightforward: it is sufficient to construct a uniform grid in (c^0, c^1) . The grid spacing Δc is chosen in the same way as in [1, 18], and listed in the third column of Tab. I. In Fig. 3 we show the effectualness tests for the same three banks of Fig. 2. As in Ref. [1],

¹ The code is available at https://github.com/JayWadekar/gwIAS-HM.

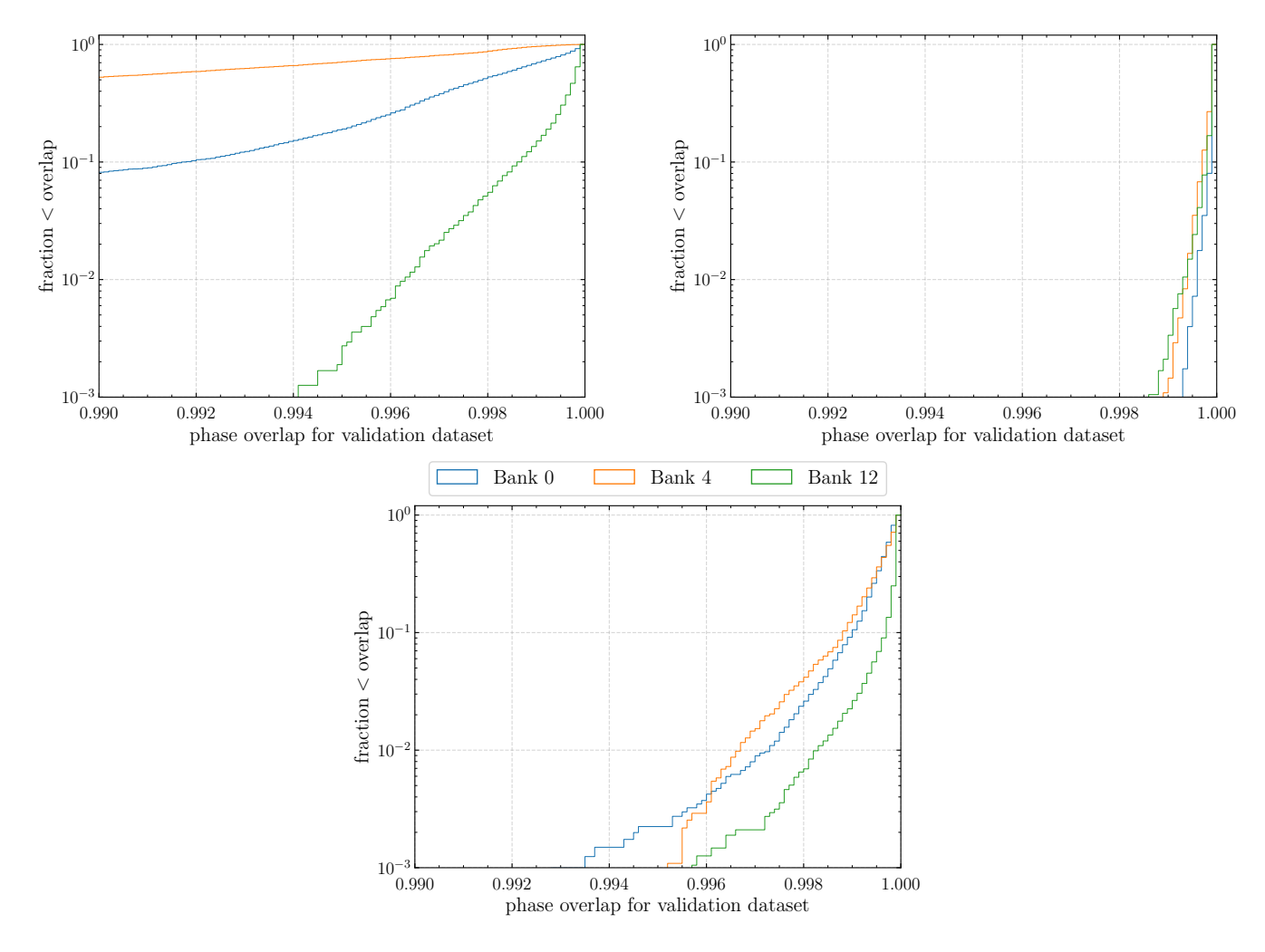


FIG. 2: Phase overlap of Eq. (3) between the validation phases and their model via random forest (upper right panel) and autoencoder (lower panel) in the selected banks BBH-0, $\mathcal{M} \in [2.6, 5.3] \, M_{\odot}$ (Bank 0), BBH-4, $\mathcal{M} \in [5.8, 10.8] \, M_{\odot}$ (Bank 4) and BBH-12, $\mathcal{M} \in [28.4, 173.5] \, M_{\odot}$ (Bank 12). We see that in all three cases the random forest achieves an excellent reconstruction of the phases: less than 0.1% of the validation waveforms are reconstructed with an error larger than 0.1%. In the autoencoder case, instead, we see that a fraction between 2% and 10% of validation waveforms have reconstruction error larger than 0.1%. The upper left panel shows instead the phase overlap between the validation phases and their reconstruction keeping only the first 2 SVD coefficients. We see that both autoencoder and random forest greatly outperform this simple dimensionality reduction in the low-mass case. In the high-mass regime, instead, it is only the random forest that performs significantly better.

for each test waveform we first unwrap its phase and take the dot product with the phase basis functions of Eq. (1) to find the $(c_{\text{test}}^0, c_{\text{test}}^1)$ coefficients of this test waveform. Then, we find the closest grid point $(c_{\text{closest}}^0, c_{\text{closest}}^1)$ in the (c^0, c^1) space, and construct the 22 mode using again Eq. (1) but with $(c^0, c^1) = (c_{\text{closest}}^0, c_{\text{closest}}^1)$ and $(c^2, c^3, \dots c^9) = \text{RF}(c_{\text{closest}}^0, c_{\text{closest}}^1)$. Then, we calculate the match with the test waveform. We can then also compare this with the match obtained if we put $(c^2, c^3, \dots c^9)$ to zero.

In principle, to refine this calculation, one could take the inner product of the test waveform with all the templates in the bank and find the best match. Instead of doing this, we refine our effectualness calculation by matching the test waveforms to their closest grid points on a new and refined grid with spacing $\Delta c \to \Delta c/2$. Finally, let us recall that along the (c^0, c^1) dimensions not all the points of the rectangular grid describe physically viable waveforms. Also here, like in [1], we use the method adopted in [18] of rejecting the grid points which do not have a physical waveform in their vicinity: for reference, see Fig. 4 of [18]. The second column of Tab. I shows the number $N_{\text{templates}}$ of templates,

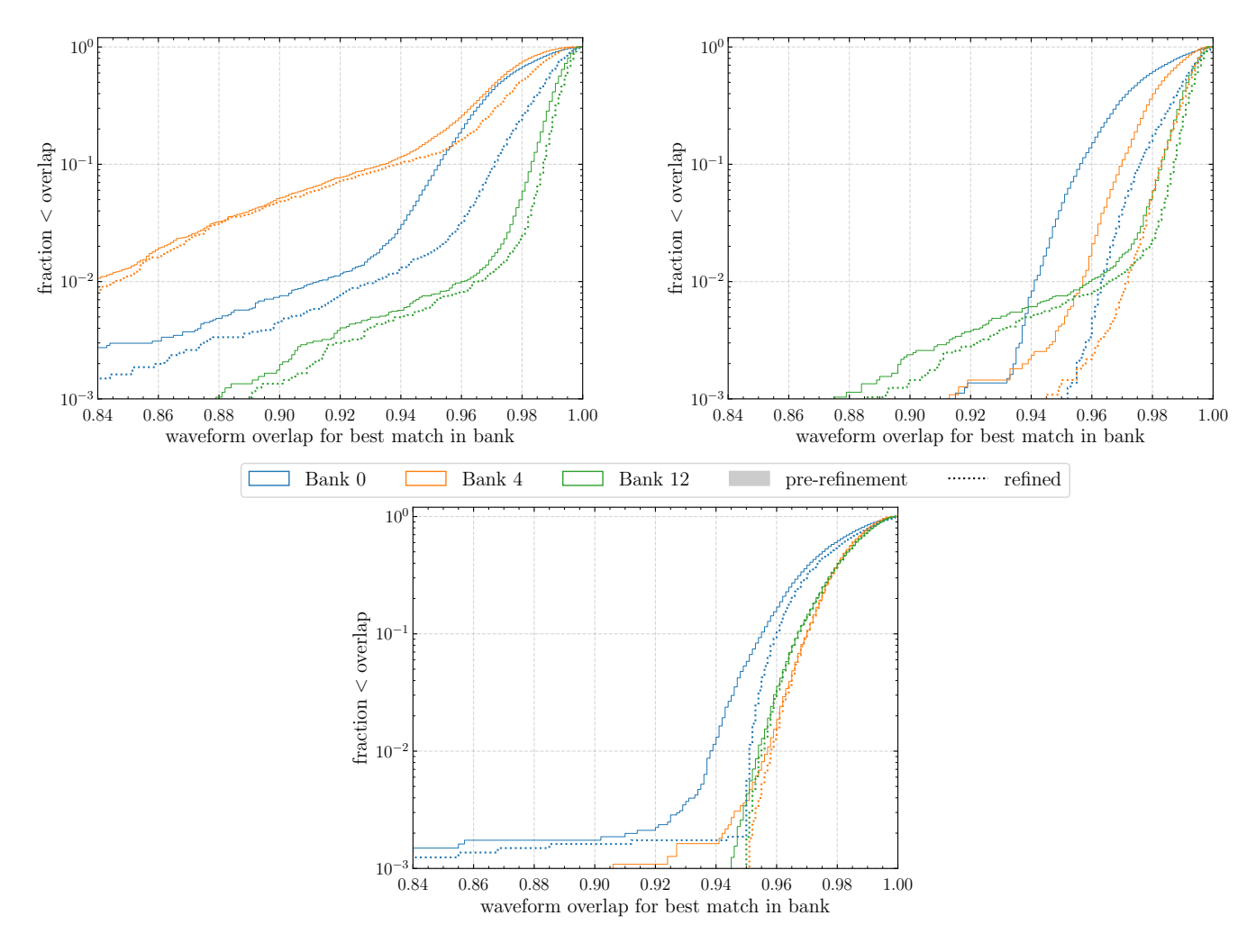


FIG. 3: Effectualness of our template banks for the simple SVD dimensionality reduction $(c^2, c^3, \dots c^9) = (0, 0, \dots 0)$ (upper left panel), the random forest case (upper right panel) and the autoencoder case (lower panel). The full bars (dotted lines) show the result before (after) grid refinement. As discussed in the main text, for the autoencoders the grid size in the latent space is given by $\Delta e = \Delta c/\mathcal{N}$, where the normalization factor \mathcal{N} was introduced at the stage of data preparation for the training of the autoencoders by rescaling the SVD components $c^A \to c^A/\mathcal{N}$. We see that generally the autoencoder performs better than the random forest in matching the test waveforms, especially after grid refinement, apart from the lowest-mass bin.

i.e. how many of these grid points are physical for each bank and sub-bank.

In the next section we carry out the template bank construction and effectualness analysis for the same banks but using autoencoders, which will require a bit of modifications in the construction of the template grid as we hinted at in Section 1.

2.2. Dimensionality reduction with autoencoders

To start, we need to train the autoencoders to model the phases in each bank and sub-bank. We follow these steps:

• first, we rescale the data c^A , $A = 0, \dots 9$ by the standard deviation of the first SVD component c^0 (we rescale both training and validation data, and we use half the phases in each sub-bank for training and half for validation). It is generally advisable to rescale the input data to zero mean and unit standard deviation as it helps with efficient

Bank	$\mathcal{M}_{\mathrm{bin\ edges}}$ $[M_{\odot}]$	Δc	N _{templates} in sub-banks (SVD2, RF)	$N_{\rm templates}$ in sub-banks (autoencoder)
BBH-0	2.6, 5.3, 6.8, 8.4, 10.7, 19.8	0.55	10442,1702,774,465,280	9806,1621,724,422,250
BBH-1	5.8, 11.9, 15.8, 27.3	0.5	1902, 318, 157	1842, 295, 123
BBH-2	8.9, 18.5, 23., 38.6	0.45	755, 94, 55	726, 72, 44
BBH-3	12.,22.4,27.4,49.6	0.45	263, 53, 44	240, 36, 33
BBH-4	5.8, 10.8, 13.5, 19.5	0.4	1782, 422, 225	1773, 398, 206
BBH-5	14.7, 23.9, 30.3, 64.2	0.35	174, 67, 63	181, 56, 39
BBH-6	10.3,21.,29.5,75.9	0.3	249, 115, 76	209, 96, 61
BBH-7	12.9, 30.6, 92.4	0.25	145, 74	114, 74
BBH-8	15.1 39.9, 108.3	0.25	73, 31	47, 31
BBH-9	18.5, 127.3	0.35	37	15
BBH-10	21.1, 149.1	0.3	19	13
BBH-11	24.7, 168.6	0.3	14	7
BBH-12	28.4, 173.5	0.3	5	3
BBH-13	32.6, 173.8	0.3	6	2
BBH-14	37.8, 173.6	0.3	3	1
BBH-15	43.2, 173.7	0.25	3	1
BBH-16	51.8, 166.	0.2	3	1
Total			20890	19562

TABLE I: Details of the 22 template banks. The banks are split according to 22 amplitudes – see Fig. 4 of [1] – and the sub-banks are split according to the chirp mass (\mathcal{M}) . The lower and upper bin edges in \mathcal{M} are given in the second column. From BBH-9 onwards, we only have a single sub-bank per bank. Δc denotes the grid size in the (c^0, c^1) space that is used to generate the templates. The last two columns show the number of templates we have according to the technique we use for the dimensionality reduction of the space of SVD coefficients. The second-to-last column shows the number of templates we have if we switch on only the 2 lowest-order SVD coefficients ("SVD2") or use random forests to model the higher-order ones. The last column instead shows the number of templates we have if we use autoencoders with the method discussed in Section 2.2. We see that the latter results in a slightly lower number of templates than the first two.

training of the network: this is our motivation behind rescaling c^A . We call this normalization factor \mathcal{N}^2 ;

• we construct in pytorch an autoencoder $10 \xrightarrow{\mathcal{E}} 2 \xrightarrow{\mathcal{D}} 10$ to learn the manifold of the $\{d^A\} = \{c^A/\mathcal{N}\}$. We consider a simple architecture where \mathcal{E} and \mathcal{D} are both MLPs (Multi-Layer Perceptrons) with 4 hidden layers, each with 64 neurons activated by the Gaussian Error Linear Unit (GELU) function. Hence, our model for the manifold of the proper SVD components $\{c^A\}$ is given by

$$c_{\text{model}}^A = \mathcal{N} \, \mathcal{D}^A(e^0, e^1) \,\,, \tag{4}$$

where it is important to emphasize the presence of the multiplicative factor \mathcal{N} on the right-hand side;

• when we train the autoencoder, we need to impose the preservation of distances between embedding and latent space, i.e. we have $L = \alpha \times L_{\text{reconstruction}} + \beta \times L_{\text{distance preservation}}$. We use the following loss functions (we denote

 $^{^2}$ We are aware that to avoid leakage one should define $\mathcal N$ using only the training data.

 $\mathcal{D}^A(\mathcal{E}(d_{\text{train}}))$ by $\tilde{d}_{\text{train}}^A$ here)

$$L_{\text{reconstruction}} = \text{MSE}(d_{\text{train}}, \tilde{d}_{\text{train}})$$
 (5)

$$L_{\text{distance preservation}} = \frac{2}{N_{\text{train}}(N_{\text{train}} - 1)} \sum_{i < j} e^{-\frac{|d_{\text{train}}^{(ij)}|}{\gamma}} \left(|d_{\text{train}}^{(ij)}| - |e_{\text{train}}^{(ij)}| \right)^2, \tag{6}$$

where MSE is the usual mean squared error reconstruction loss and

$$|d_{\text{train}}^{(ij)}| = |d_{\text{train}}^{(i)} - d_{\text{train}}^{(j)}| \quad \text{and} \quad |e_{\text{train}}^{(ij)}| = \sqrt{\delta_{\mu\nu} \left[\mathcal{E}^{\mu}(d_{\text{train}}^{(i)}) - \mathcal{E}^{\mu}(d_{\text{train}}^{(j)})\right] \left[\mathcal{E}^{\nu}(d_{\text{train}}^{(i)}) - \mathcal{E}^{\nu}(d_{\text{train}}^{(j)})\right]}$$
(7)

We train the autoencoders for all banks and sub-banks using $\alpha=\beta=1$. Since we are interested in preserving only small distances we choose $\gamma=1$ (recall that the goal is to find a coordinate system where the metric is as close as possible to being flat across the whole manifold: in order to find this coordinate system – assuming that it exists – it is sufficient to impose that only the distance between neighboring points is preserved). Notice that when we make a plot of embedding-space versus latent-space distances we need to show $\mathcal{N}|e_{\mathrm{valid}}^{(ij)}|$ on the y axis if on the x axis we plot $|c_{\mathrm{valid}}^{(ij)}| = |c_{\mathrm{valid}}^{(i)} - c_{\mathrm{valid}}^{(j)}|$. We see from Fig. 4 that distances are preserved extremely well. A straightforward check, whose result we do not show here because it would be redundant with Fig. 4, is to check that the induced metric

$$g_{\mu\nu} = \mathcal{N}^2 \delta_{AB} \frac{\partial \mathcal{D}^A}{\partial e^\mu} \frac{\partial \mathcal{D}^B}{\partial e^\nu} \tag{8}$$

is extremely well approximated as $g_{\mu\nu} \approx \mathcal{N}^2 \delta_{\mu\nu}$.

The reconstruction error of the autoencoder is shown in Fig. 2. We see that the autoencoder performs worse than the random forest: however, we emphasize that we have not refined the training of our autoencoders after the initial pass (in view of future use in the IAS search pipeline, we trained them once for all banks and sub-banks, with the idea that they can be refined at a future time), and we trained all of them in torch.float32 precision (which can also be refined at a future time). Even so, we will see in a moment that even with this difference in reconstruction the autoencoders perform slightly better than the random forests in the effectualness tests.

In order to construct the actual templates in the autoencoder case we need to adapt the geometric placement method of [18]. We first construct a uniform grid in the embedding space: since we know that the induced metric is very well approximated by $\mathcal{N}^2\delta_{\mu\nu}$, in order to achieve a spacing Δc in the embedding space we need our grid to have spacing $\Delta e = \Delta c/\mathcal{N}$. The grid is centered at $\mathcal{E}(d^0=0,d^1=0,\ldots d^9=0)$: in other words, it corresponds to the mean phase across the sub-bank. Then, we proceed as in the random forest case. For each test waveform we extract its SVD components, we encode them, and we find the closest grid point in the latent space: the waveform that matches the test one is then constructed by decoding this grid point. The only remaining problem to address is how to determine which grid points represent physical waveforms and which do not. In order to do this, we train a simple normalizing flow in zuko⁴ for each bank to predict the distribution of points (the encoding of the examples we used to construct our c^A dataset) in the latent space, and then we drop all grid points that are outside the 99.7% CL contour of this distribution. The last column of Tab. I lists the number of templates obtained with this procedure, while Fig. 5 shows an example of the latent- and embedding-space distribution of points for Bank 0 and Bank 4. As in the previous section, we also implement a refinement procedure by constructing a grid with a smaller grid spacing.

When investigating different choices of hyperparameters for Bank 0, we tried optimizing the choice of γ using Simulated Annealing, with an exponential cooling schedule for the temperature $(T_k = T_0 \cdot \text{cooling_rate}^k)$, with starting temperature of order of the validation loss of an initial pre-annealing run with $\gamma = 1$), and a log-uniform perturbation to propose candidate γ values $(1/\gamma_{\text{new}} = 1/\gamma_{\text{current}} + 10^U)$, where $U \sim \text{Uniform}(-2, 1)$. Even experimenting with different cooling rates and number of epochs for the annealing, we have not found significant improvements in the distance preservation: hence, since we planned to train at once all banks and sub-banks, we fixed $\gamma = 1$ throughout all our trainings.

⁴ We use an unconditional Neural Spline Flow (NSF) [19] with 2 input features and 4 layers of transforms, each transform's internal neural network having 2 hidden layers of 64 neurons. Notice that the NSF spline transformations are defined over the domain [-5, 5] (see here for the zuko implementation): since our features lie in this box for all banks and sub-banks we do not standardize features before training.

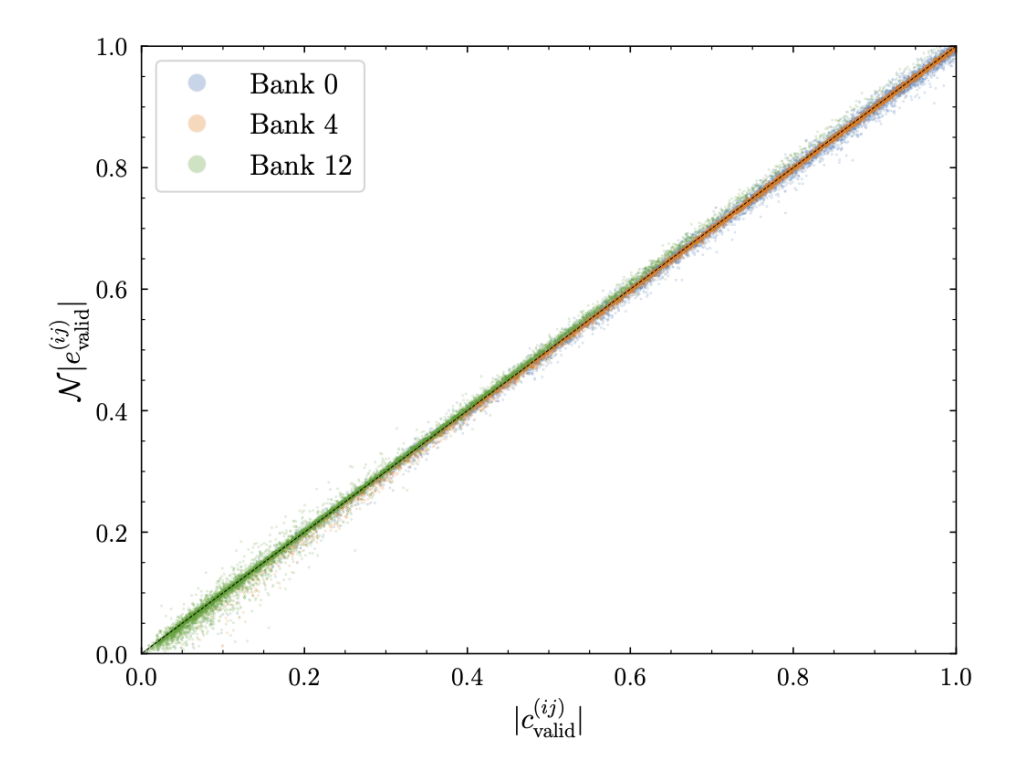


FIG. 4: Scatter plot of the distances in the embedding space vs. the Euclidean distances in the latent space for 1% of the pairs of validation points for the three banks discussed in Section 2.2. We see that the distances are preserved extremely well in this case, at variance with the example of a unit sphere. Notice that for each of the three banks we plot only 10000 randomly-chosen pairs of points among those having a distance $|c_{\text{valid}}^{(ij)}| \leq 1$ in the embedding space. This is done only to allow the reader to distinguish the three colors in the plot: including all pairs would still show the points clustering extremely close to the diagonal.

Instead of re-running the matching procedure for all test waveforms, we consider only those waveforms whose match with a template on the un-refined grid is less than 0.95: for these waveforms we try to find a new match on a refined grid $\Delta e \to \Delta e/2$. The effectualness test is shown in the lower panel of Fig. 3: we see that the autoencoder performs slightly better than the random forest in the case of high-mass banks, for which after refinement all test waveforms are reconstructed with an overlap larger than 0.95 unlike the random forest case.

Before concluding, it is interesting to discuss the curvature of the banks. Post-facto, we can conclude that Bank 0, Bank 4 and Bank 12 have all negligible curvature, since for all of them we were able to find a distance-preserving coordinate chart. That is, we have seen that for all the three banks considered, the induced metric is very well approximated by $\mathcal{N}^2\delta_{\mu\nu}$. Is there a case among all our banks and sub-banks where the situation is different than this? In principle, given the high codimension of our isometric embeddings, there is no particular constraint on the size of the intrinsic curvature of our manifolds. However, we find that all our banks and sub-banks have small or negligible curvature. We discuss this further in the appendices.

3. CONCLUSIONS

In this paper we have generalized the non-linear compression of geometric-placement template banks of [1] for (2,2)-only GW waveforms to use autoencoders instead of random forests. We have shown that, even if our autoencoders have not been refined to perform better than the random forests in predicting the phases of the GW waveforms in each bank and sub-bank – our autoencoders perform not as well as the random forests in predicting the SVD coefficients that describe the phases of waveforms in each bank and sub-bank [18] – the template banks we obtain show in general

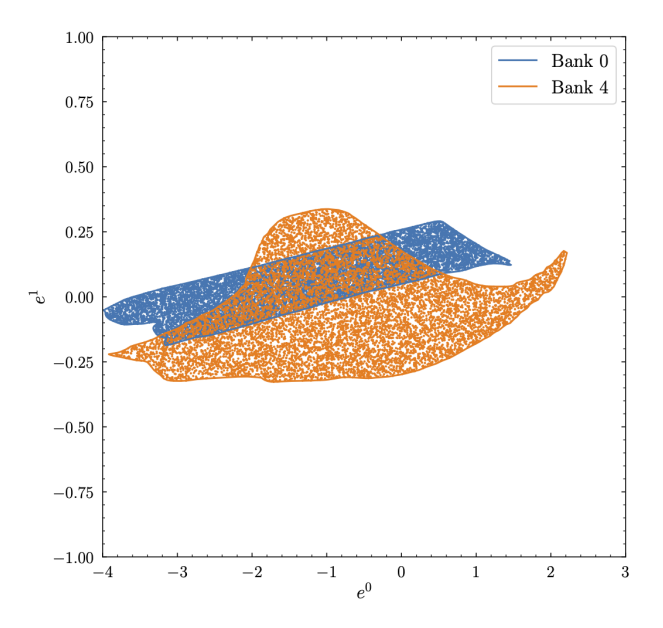


FIG. 5a: A collection of 10000 random points within the 99.7% CL contour of the distribution of latent-space points for Bank 0 and Bank 4.

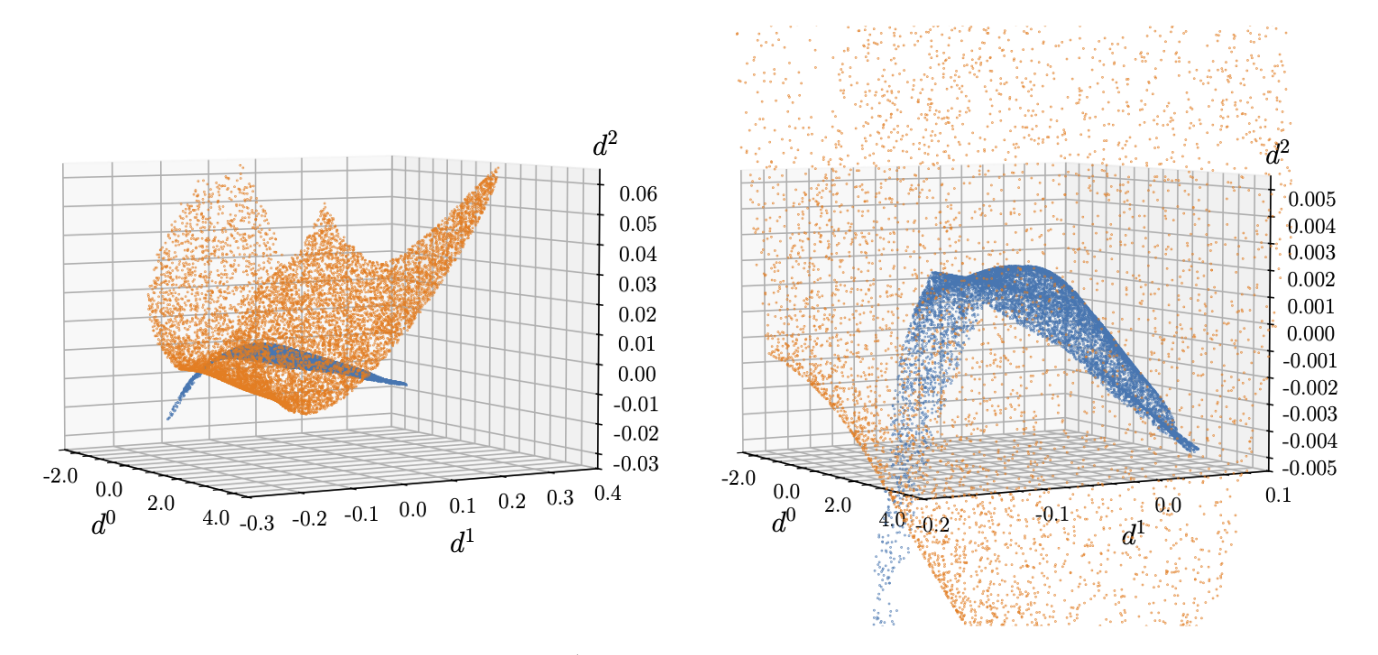


FIG. 5b: The first three components of the decoded d^A (see Eq. (4) for their definition) for the 10000 latent-space points shown in Fig. 5a. The right panel is a zoomed-in version of the left panel.

comparable effectualness as those of [1], and are actually slightly more effectual at the high-mass end than those of that reference. Moreover, our template banks achieve this effectualness while having a slightly smaller number of templates than [1] across the whole mass range. Future directions might include extending our method to include higher modes as in [1], and implementing these template banks in the actual IAS search pipeline.

Importantly, our geometric placement method with autoencoders relies on us being able to find a coordinate system where the metric is $\approx \mathcal{N}^2 \delta_{\mu\nu}$ across the whole manifold. This might not be possible if the banks have nonzero curvature, comparable to the grid spacing $\Delta c/\mathcal{N}$. In this case an alternative, albeit much more complex to implement,

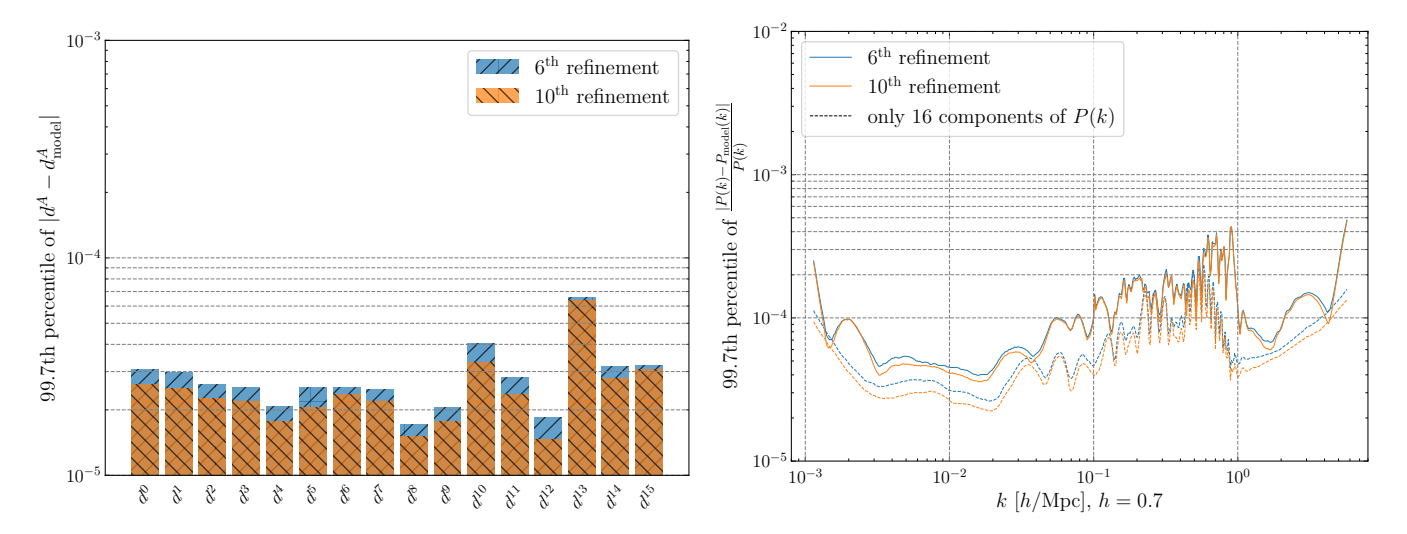


FIG. 6: Our decoder \mathcal{D} aims at reconstructing the rescaled SVD coefficients $d^A = c^A/\mathcal{N}$. In order to achieve the necessary precision we first trained 5 teachers using the simple reconstruction loss MLP(d_{train} , \tilde{d}_{train}), where $\tilde{d}_{\text{train}}^A = \mathcal{D}(\theta_{\text{train}})$ and θ_{train} are the cosmological parameters (ω_c, ω_b, n_s) (each batch of the training dataset contains a random selection of cosmological parameters from the regular grid used to generate the training spectra). Then, we trained a student with the same architecture as the 5 teachers using transfer learning: the loss was the sum of a reconstruction loss MLP(d_{train} , $\tilde{d}_{\text{train}}^{\text{student}}$) and MLP($d_{\text{train}}^{\text{train}}$), where $d_{\text{train}}^{\text{train}}$ is the mean of the predictions of the 5 teachers. Following the initial transfer learning procedure, the student model was iteratively fine-tuned for ten subsequent iterations. All the training procedure was carried out using torch.float64 precision. The left panel shows the 99.7th percentile of the absolute error for each of the 16 d^A in the validation set, for the fifth-to-last and last refinement. The right panel shows instead the 99.7th percentile of the relative error in the validation power spectra as a function of wavenumber. By comparing the full with the dashed lines (the dashed lines showing the error with respect to the validation spectra where all the SVD components after the 16th are set to zero) shows that we are mostly dominated by the error coming from us keeping only the first 16 basis functions.

direction one could investigate is the following:

- 1. first we train the autoencoder to reach a given level of precision in the reconstruction of the manifold;
- 2. then, since we have the possibility of computing the distance $D(e_{(i)}, e_{(j)})$ between any two points on the manifold by solving the geodesic equation, we can construct for a set of random points $\{e_{(i)}\}$ the functional

$$\sum_{i < j} \frac{1}{D(e_{(i)}, e_{(j)})^{\alpha}} ; \tag{9}$$

3. minimizing this functional should organize the points $\{e_{(i)}\}$ in a "grid" that is likely not uniform, but is such that all neighboring points have around the same geodesic distance from one another.

For this it could be beneficial, after having trained the autoencoder, to find a coordinate change e = e(e') (i.e. $c_{\text{model}} \propto \mathcal{D}(e(e'))$ is the decoder now) such that the e' lie on a domain that is easier to deal with than those seen e.g. in Fig. 15. This can be achieved with the invertible transformations typically used to train normalizing flows. Even then, successfully implementing this method requires to deal with a lot of unknown variables, be it the choice of what power α of the inverse geodesic distance to put in Eq. (9), the fact that it is not known in advance at which distance the points will stabilize (this likely being a function of how many points we start with), and last but not least the fact that computing the geodesic distance on curved manifolds is not an easy task in general and an area of

active research.⁵

We conclude by discussing the possibility of performing dimensionality reduction using autoencoders in the space of another set of SVD coefficients, this time in the context of cosmology. More precisely, we have in mind the COBRA decomposition of the linear matter power spectrum of Ref. [21]. One can generate a set of linear power spectra as a function of a number of cosmological parameters (ω_c , ω_b and n_s , for example), and construct its SVD to find a small number of basis functions with which to represent any linear power spectrum. More precisely, following Ref. [21] we generate power spectra at 500 wavenumbers between $0.8 \times 10^{-4} \,\mathrm{Mpc}^{-1}$ and $4 \,\mathrm{Mpc}^{-1}$ on a regular $(40 \times 20 \times 20)$ grid $(\omega_{c}, \omega_{b}, n_{s}) \in [0.08, 0.175] \times [0.020, 0.025] \times [0.8, 1.2]$ using CAMB (see the last column of Tab. 1 of [21] for more details), and we extract the first $16 c^A$ as in Ref. [21] (with the difference that besides rescaling the power spectra by the mean of the templates, we also subtract the mean of these rescaled spectra before performing the SVD): this is our training set. Then, we uniformly generate 32256 random validation spectra in the same ω_c , ω_b and n_s , range. There are two differences with the GW case discussed in this paper. First, now we would like that the latent space is the space of cosmological parameters $(\omega_c, \omega_b, n_s)$, effectively finding the "inverse" of the Boltzmann code used to generate the templates. This is less trivial than just autoencoding the c^A as done in this paper. Second, Ref. [21] only generated templates on an uniform and structured grid, without a notion of distance between the resulting spectra or the space of the c^A , unlike e.g. what was discussed in Ref. [22] in the context of cosmology. Hence, we are not interested – when comparing with Ref. [21] – in constructing distance-preserving autoencoders. In Fig. 6 we show a preliminary result for what we could call the training of the decoder only: we construct a simple MLP with a 3-dimensional input layer, 8 hidden layers each containing 128 neurons and a GELU activation, and a 16-dimensional output layer, and train it to reconstruct $d^A = c^A/\mathcal{N}$ where \mathcal{N} is defined as in Section 2.2.6 We refer to the caption of Fig. 6 for more details about the training. While our result can already be used as an alternative to the Radial Basis Function (RBF) interpolation of [21] – we checked that it has comparable speed (e.g. we can predict our 32256 validation spectra in $\sim 660\,\mathrm{ms}$ on a single core) while having slightly better precision (compare the magenta line in the lower panel of Fig. 1 of [21] with the right panel of Fig. 6) – it will be interesting to check if we can construct an autoencoder for the 16 SVD coefficients using this MLP as starting point for the decoder, and to investigate in which sense distance-preserving can be useful in cosmology. We present preliminary results in Appendix F and we leave a more detailed investigation to future work.

Acknowledgments — GC acknowledges support from the Institute for Advanced Study where part of this work was carried out. We thank Lorenzo Bordin for useful comments. We thank Thomas Bakx for providing the dataset "Plin_CAMB_LCDM_Wide.dat" we used as training dataset for the COBRA autoencoder and for providing the code used in Ref. [21] to get the SVD of the linear matter power spectra templates. We acknowledge use of the numpy, scipy, pytorch, zuko, scikit-learn and matplotlib packages.

APPENDIX

In the Appendix we discuss different results that were not of crucial importance for the main text, but that are nevertheless interesting to understand the geometry of our template banks. Appendix F, instead, contains some preliminary results on the COBRA autoencoder.

where $e^{\mu}(\lambda)_{\Phi} = e^{\mu}_{(j)}\lambda + (1-\lambda)e^{\mu}_{(i)} + \lambda(1-\lambda)\text{MLP}^{\mu}(\lambda)_{\Phi}$. Finding the optimal weights Φ of the MLP, initializing them such that the MLP vanishes, will find both the geodesic curve and, from it, $D(e_{(i)}, e_{(j)})$. Knowledge of the Christoffel symbols and the formulas of Appendix A could be used to inform better the form of $e^{\mu}(\lambda)_{\Phi}$ at the boundaries and accelerate convergence. Moreover, we notice that having the Christoffel symbols in pytorch as in Appendix A allows us to perform random geodesic walks on the manifold with a constant – albeit small – step, such that every point is at a fixed geodesic distance from the preceding one [20]. However these points will not be distributed uniformly but according to the volume form on the manifold and, most importantly, this would not be a geometric but a stochastic placement of templates.

⁵ Notice that, given that our metric is already in pytorch, one could try to compute $D(e_{(i)}, e_{(j)})$ by minimizing over Φ the functional $\frac{1}{2} \int_0^1 \mathrm{d}\lambda \, g_{\mu\nu} \left(e(\lambda)_\Phi \right) \frac{\mathrm{d}e^\mu(\lambda)_\Phi}{\mathrm{d}\lambda} \, \frac{\mathrm{d}e^\nu(\lambda)_\Phi}{\mathrm{d}\lambda} \; , \tag{10}$ where $e^\mu(\lambda)_\Phi = e^\mu_{(j)}\lambda + (1-\lambda)e^\mu_{(i)} + \lambda(1-\lambda)\mathrm{MLP}^\mu(\lambda)_\Phi$. Finding the optimal weights Φ of the MLP, initializing them such that the

 $^{^6}$ Unlike Section 2.2, here ${\mathcal N}$ is defined using only training data.

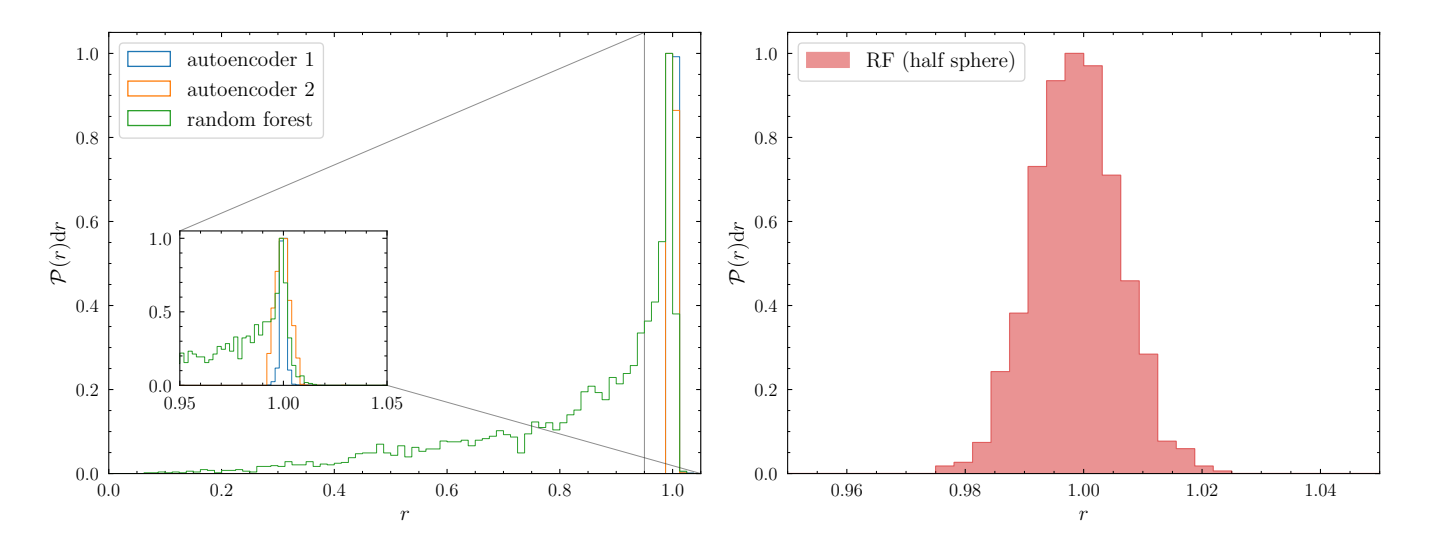


FIG. 7: Left panel: histogram of validation radii $r = |\mathbf{x}|$ (where $\mathbf{x} = (x_{\text{valid}}, y_{\text{valid}}, \text{RF}(x_{\text{valid}}, y_{\text{valid}})$ for the random forest and $\mathbf{x} = \mathcal{D}(\mathcal{E}(\mathbf{x}_{\text{valid}}))$ for the two autoencoders). Right panel: histogram of r for the random forest in the case of the half sphere.

A. Toy example: embedding a sphere

It is always instructive to consider some examples that are well understood. We start with the unit sphere S^2 isometrically embedded in 3-dimensional Euclidean space. We generate 8192 points on the sphere using the Fibonacci sphere algorithm [23], and randomly split half of them in training and validation sets. We imagine that the coordinates $\mathbf{x} = (x, y, z)$ play the role of the first 10 SVD coefficients c^A , $A = 0, \dots 9$ for GW waveforms discussed in the introduction, and that we want to describe this 2-dimensional manifold using dimensionality reduction techniques. It is clear that, in this particular example (where by construction we do not have any hierarchy between x, y or z, since we only "postulated" that these come from a SVD), a dimensionality reduction consisting in taking only 2 of the three "SVD coefficients" (i.e. only x and y, or only y and z, etc.) would completely fail to capture the manifold, hence we immediately move to other methods. Inspired also here by Ref. [1] and by the main text, we then train a random forest (also here we use https://scikit-learn.org/stable/modules/generated/sklearn.ensemble. RandomForestRegressor.html, with 50 trees and maximum depth of 50) to predict the z coordinate as a function of (x,y). We plot the result in the left panel of Fig. 7. We see that the random forest makes an extremely poor job of describing S^2 . The reason is that for any given (x,y,z) with unit norm, also (x,y,-z) has $|\mathbf{x}|=1$, and the random forest cannot capture this. This is confirmed by the right panel of Fig. 7, where we use a random forest with the same architecture to predict z = RF(x,y) but only for $z \geq 0$: the random forest manages to fit the half sphere just fine.

We can then train an autoencoder $3 \xrightarrow{\mathcal{E}} 2 \xrightarrow{\mathcal{D}} 3$ to learn a coordinate chart $\mathbf{x} = \mathbf{x}(e^0, e^1)$ for S^2 . At variance with the random forest case, we now want to find a way to enforce that distances in the latent space are equal to distances in the embedding space (Euclidean distances $|\delta \mathbf{x}|$ between points on the unit sphere): this is because, as discussed in Section 1, we are focusing on autoencoders that we can use in the GW analysis pipeline with geometric placement. Once we have the decoder \mathcal{D} , recalling the formula for the induced metric

$$g_{\mu\nu} = \delta_{IJ} \frac{\partial \mathcal{D}^I}{\partial e^{\mu}} \frac{\partial \mathcal{D}^J}{\partial e^{\nu}} , \tag{11}$$

we see that the requirement of distances in the latent space being equal to distances in the embedding space is equivalent to asking that $g_{\mu\nu} \approx \delta_{\mu\nu}$, and it can be imposed at two different levels:

⁷ Let us recall that the sphere is not coverable by a single atlas. Even the standard θ , ϕ coordinates fail at the poles (which are nevertheless sets of zero measure).

- 1. we can ask that the equality holds around a point;
- 2. we can ask that it holds globally on the sphere.

It is always possible to satisfy 1 (we would just be looking for a Riemann coordinate system at that point), but it is never possible to satisfy 2 due to the curvature of the sphere (a Riemann patch will have size of at most $\sim 1/\sqrt{2}$, recalling that for S^2 the Ricci scalar R is equal to 2).

Nevertheless, let us try to train an autoencoder in pytorch that satisfies 2, to see that this is not possible: as an example, we consider a simple architecture where \mathcal{E} and \mathcal{D} are both MLPs with 4 hidden layers, each with 64 neurons activated by the GELU function. As loss function we again use $(\tilde{x}_{\text{train}}^{I} = \mathcal{D}^{I}(\mathcal{E}(\boldsymbol{x}_{\text{train}})))$ in the equation below)

$$L = \alpha \times L_{\text{reconstruction}} + \beta \times L_{\text{distance preservation}}$$

$$= \alpha \times \text{MSE}(\boldsymbol{x}_{\text{train}}, \tilde{\boldsymbol{x}}_{\text{train}}) + \beta \times L_{\text{distance preservation}}.$$
(12)

Here the first term is a simple reconstruction loss for the autoencoder, while the distance-preservation loss is given by

$$L_{\text{distance preservation}} = \frac{2}{N_{\text{train}}(N_{\text{train}} - 1)} \sum_{i < j} e^{-\frac{|\boldsymbol{x}_{\text{train}}^{(ij)}|}{\gamma}} \left(|\boldsymbol{x}_{\text{train}}^{(ij)}| - |\boldsymbol{e}_{\text{train}}^{(ij)}| \right)^2, \tag{13}$$

where

$$|\boldsymbol{x}_{\text{train}}^{(ij)}| = |\boldsymbol{x}_{\text{train}}^{(i)} - \boldsymbol{x}_{\text{train}}^{(j)}| \quad \text{and} \quad |e_{\text{train}}^{(ij)}| = \sqrt{\delta_{\mu\nu} \left[\mathcal{E}^{\mu}(\boldsymbol{x}_{\text{train}}^{(i)}) - \mathcal{E}^{\mu}(\boldsymbol{x}_{\text{train}}^{(j)})\right] \left[\mathcal{E}^{\nu}(\boldsymbol{x}_{\text{train}}^{(i)}) - \mathcal{E}^{\nu}(\boldsymbol{x}_{\text{train}}^{(j)})\right]}$$
(14)

The hyperparameters α and β control the relative strength of the two loss functions, while γ as in Eq. (6) controls the "locality" of the distance preservation. Only distances of samples whose separation in the embedding space is of order γ are preserved: so for small γ we only preserve distances of nearby samples, while larger γ imposes the constraints through a finite domain. The results are shown in Fig. 8 for two different (random) choices of α, β, γ : we see that it is not possible to preserve distances globally on the sphere, as expected.⁸ In Appendix C, we show instead what happens if we try to satisfy 1.

It is interesting to look at the curvature of the latent space in more detail, and see how to recover the curvature of the sphere. Since we use the C^{∞} GELU activation, we can use standard formulas of differential geometry and pytorch's automatic differentiation to compute the metric of Eq. (11). From that, we can compute the Christoffel symbols

$$\Gamma^{\rho}_{\mu\nu} = g^{\rho\lambda} \delta_{IJ} \frac{\partial \mathcal{D}^I}{\partial e^{\lambda}} \frac{\partial^2 \mathcal{D}^J}{\partial e^{\mu} \partial e^{\nu}} , \qquad (15)$$

and finally the Riemann tensor $R^{\rho}_{\sigma\mu\nu} = \partial_{\mu}\Gamma^{\rho}_{\nu\sigma} - \partial_{\nu}\Gamma^{\rho}_{\mu\sigma} + \Gamma^{\rho}_{\mu\lambda}\Gamma^{\lambda}_{\nu\sigma} - \Gamma^{\rho}_{\nu\lambda}\Gamma^{\lambda}_{\mu\sigma}$. However, we have found it not so straightforward in pytorch to compute derivatives of a vector function – the decoder, in our case – past the second, which would be needed to compute the Riemann tensor. Hence we pursue a different route using the connection between holonomy and curvature, i.e. the non-Abelian Stokes theorem – see e.g. Appendix I of Ref. [24] and Ref. [25]. Let us consider the parallel propagator $P^{\mu}_{\ \nu}(\lambda,\lambda_0)$ along a path $e^{\mu}(\lambda)$, $\lambda \in [\lambda_0,\lambda_1]$. This satisfies the ODE

$$\frac{\mathrm{d}}{\mathrm{d}\lambda}P^{\mu}_{\ \nu}(\lambda,\lambda_0) = A^{\mu}_{\ \sigma}(\lambda)P^{\sigma}_{\ \nu}(\lambda,\lambda_0) \ , \quad \text{where} \quad A^{\mu}_{\ \sigma}(\lambda) = -\Gamma^{\mu}_{\rho\sigma}\big|_{e=e(\lambda)} \frac{\mathrm{d}e^{\rho}(\lambda)}{\mathrm{d}\lambda} \quad \text{and} \quad P^{\mu}_{\ \nu}(\lambda_0,\lambda_0) = \delta^{\mu}_{\ \nu} \ . \tag{16}$$

In a 2-dimensional manifold, if we consider a closed path ∂S_{ϵ} and we compute the holonomy $P^{\mu}_{\ \nu}(\lambda_1, \lambda_0) \equiv P^{\mu}_{\ \nu}(\partial S_{\epsilon})$ around that path, we have that

$$P_0^1(\partial S_\epsilon) = \frac{1}{2} \int_{S_\epsilon} d^2 e \, R(e) g_{00}(e) + \dots ,$$
 (17)

⁸ Since we know it is impossible to find a coordinate system on the sphere where the metric is flat, we did not investigate what happens if we try to change the architecture of the autoencoder.

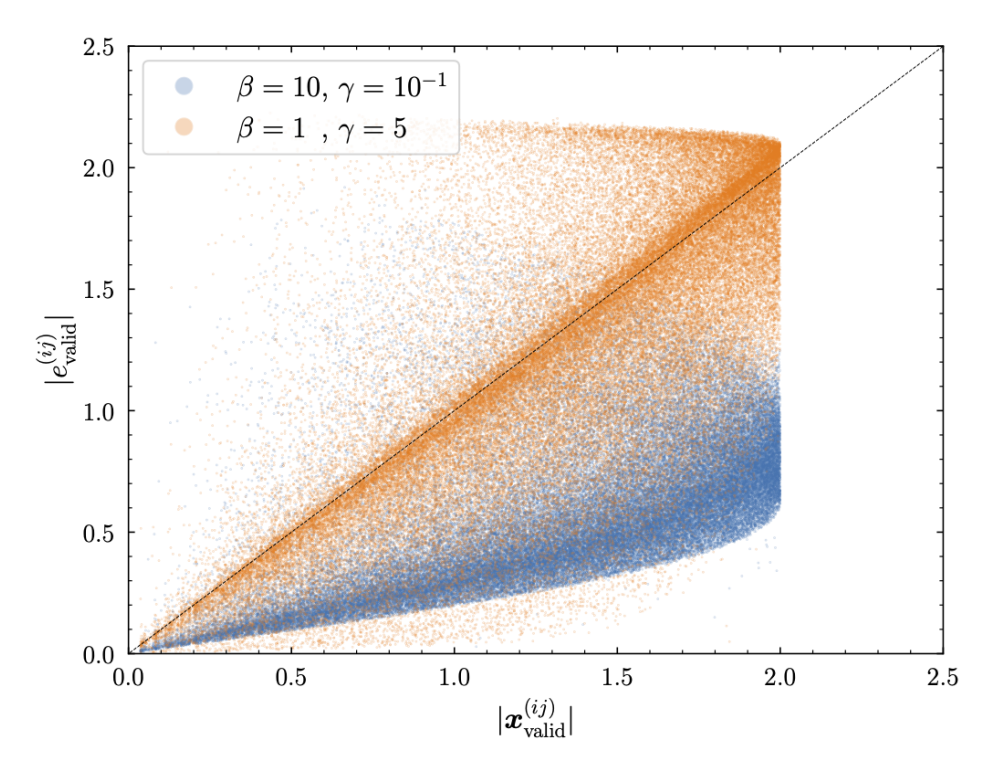


FIG. 8: Same as Fig. 4 for the autoencoder describing the unit sphere, with two different choices of the loss function hyperparameters (α – which is equal to 1 in both cases – β and γ , see Eq. 12).

where ... denote higher orders in $\int_{\mathcal{S}_{\epsilon}} d^2 e$. Hence we can define an estimator for the Ricci scalar at a point e on the manifold by considering the holonomy around a circle $\partial D_{\epsilon}(e)$ of radius ϵ centered in e:

$$\frac{R(e)}{2} \approx \frac{P_0^1(\partial D_{\epsilon}(e))}{\int_{D_{\epsilon}(e)} d^2 e' g_{00}(e')} . \tag{18}$$

In Fig. 9a we show the validation embeddings and a collection of 12288 randomly-chosen points $e \in \mathcal{S}$. This region is well inside the domain of the decoder (notice that for this experiment we consider only the autencoder trained with $\alpha = 1$, $\beta = 1$ and $\gamma = 5$, shown in orange in Figs. 7 and 8). Then, we compute the holonomy around circles of radius $\epsilon = 10^{-3}$ centered at each of these points, 9 and the integral inside the disk $D_{\epsilon}(e)$ that appears at the denominator of Eq. (18). The result is shown in Fig. 9b, where we see that the Ricci scalar is nicely distributed around the constant value R = 2 as expected, consistently with errors coming from an inexact description of the sphere, higher orders in Eq. (17), etc.

B. Toy example: embedding a cylinder

We can then discuss another example, that of a cylinder. Contrarily to the sphere this is a flat surface, so we expect to be able to find a metric-preserving autoencoder. We generate 8192 random points on a cylinder $\{x^2 + z^2 = 1, -1 \le y \le 1\}^{10}$ and, using half these points as training and half as validation, we train six different autoencoders: three with the same architecture as the sphere, and three with 8 hidden layers each with 128 neurons. Each triple was trained with the loss of Eqs. (12), (13): all have $\alpha = 1$, while β and γ are respectively $\beta = 1, \gamma = 1$,

⁹ We solve the ODE of Eq. (16) numerically, after refining the autoencoder to torch.float64 precision.

¹⁰ We can easily generate an uniform set of points by randomly sampling θ and y, since the metric is flat in these coordinates.

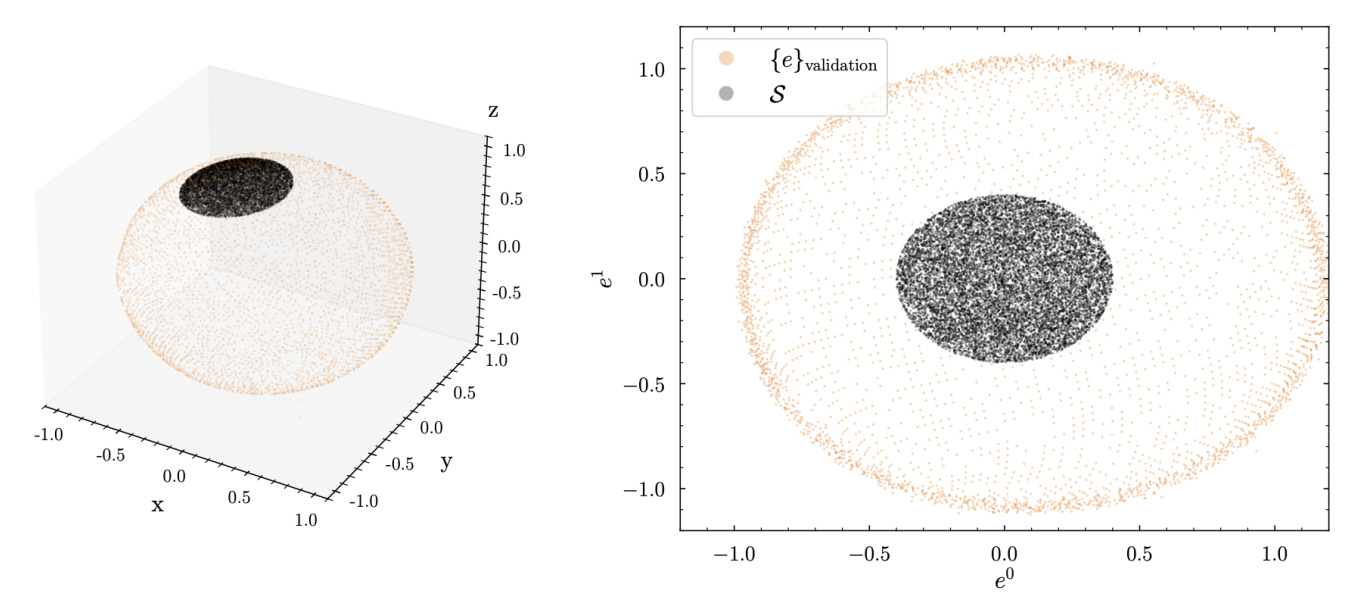


FIG. 9a: In orange we plot the validation embeddings (right panel) and corresponding decoded coordinates in Euclidean space (left panel) for the autoencoder trained with $\alpha = 1$, $\beta = 1$ and $\gamma = 5$. In black we show the 12288 randomly-selected centers $e \in \mathcal{S}$ of disks $D_{\epsilon}(e)$ with radius $\epsilon = 10^{-3}$ that we use to compute the curvature of the sphere using Eq. (18).

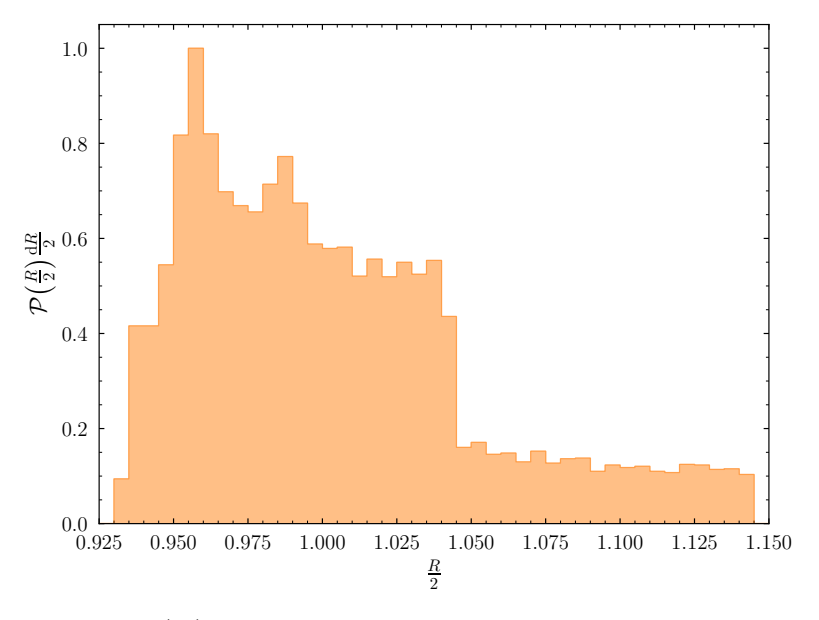


FIG. 9b: Estimates, obtained using Eq. (18), of the Ricci scalar in the region S shown in Fig. 9a. We see that the distribution is consistent with the unit sphere having a constant Ricci curvature R = 2.

 $\beta = 10, \gamma = 5$, and finally $\beta = 5, \gamma = 0.5$. The results for the two architectures are similar, so in Fig. 10 we show only the autoencoders with the same architecture as the sphere ones. While the radius is nicely fixed to 1 and y is restricted between -1 and 1 (Fig. 10a), we see that distances are not preserved even for points that are close in the embedding space (Fig. 10b). We suspect that this has to do with the fact that the cylinder, while flat, is closed and without boundary in the θ dimension. We did not investigate in detail if this is why the distance preservation of Eqs. (12), (13) fails (e.g. by trying with a half cylinder, $\theta \in [0, \pi]$), also because in the main text we have seen that in the case of GW template banks the equivalent of the loss of Eq. (13), adapted to a 10-dimensional embedding space, is

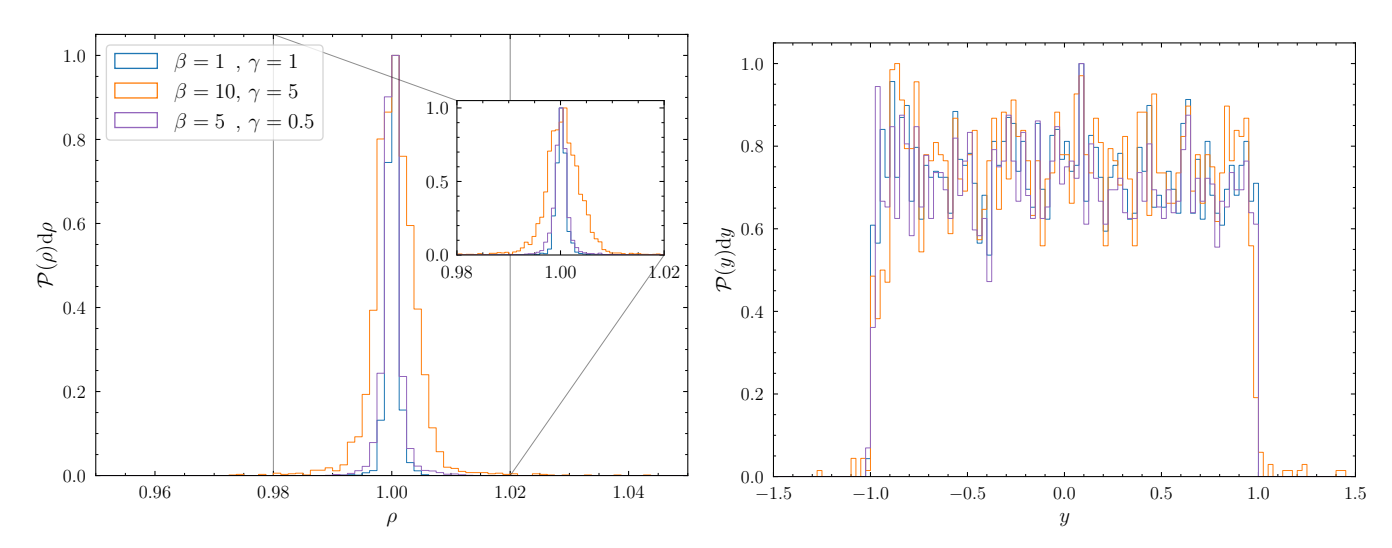


FIG. 10a: Similarly to Fig. 7, we show the histogram of validation radii $\rho = \sqrt{x^2 + z^2}$ (left panel) and of validation y coordinates (right panel) for the three autoencoders we trained to reconstruct the cylinder with the distance-preservation loss of Eq. (13). In all three cases α is equal to 1.

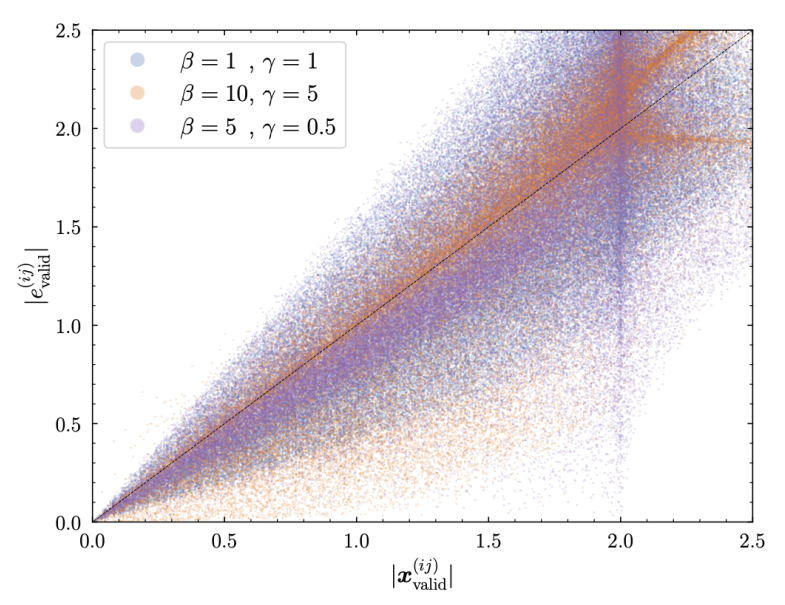


FIG. 10b: The equivalent of Fig. 8 for the cylinder example.

sufficient to obtain distance-preserving autoencoders. In Appendix D, however, we pursue a different strategy. Since the cylinder is flat, we know that we can have Riemann normal coordinates simultaneously around every point on the cylinder: hence, we implement the condition 1 on all points in the training set instead of only around a point, and we show that this allows us to find a coordinate system where the metric is $\delta_{\mu\nu}$ and distances are preserved.

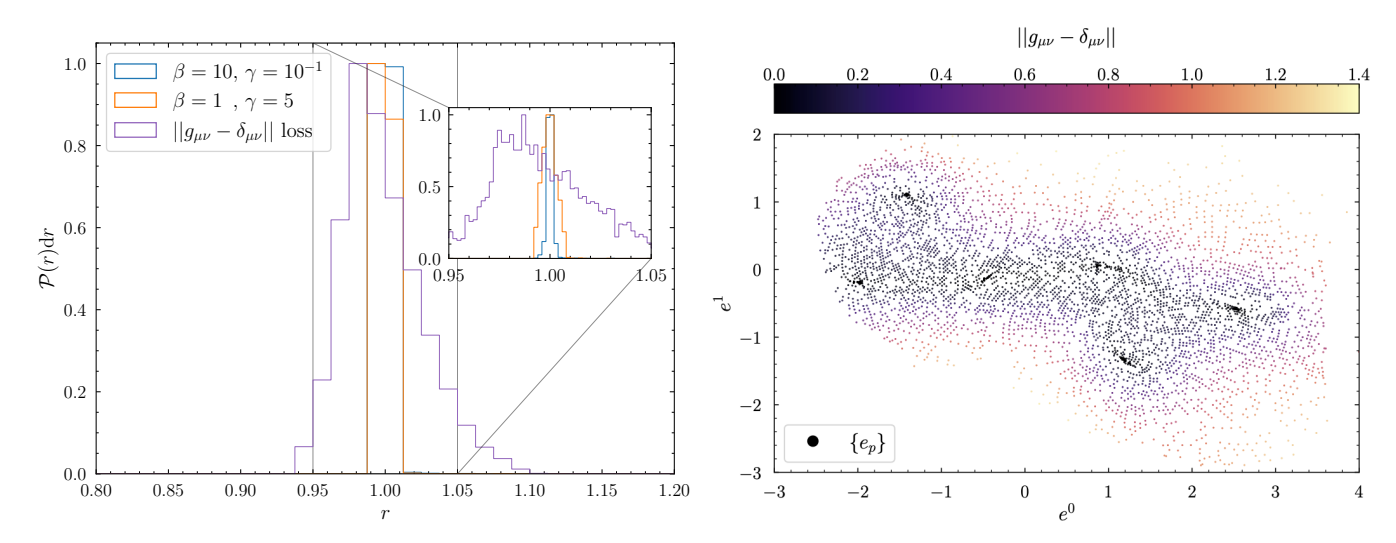


FIG. 11a: Left panel: as in Fig. 7, we show the histogram of validation radii $r = |\mathbf{x}|$ for the two autoencoders of Appendix A and the new autoencoder trained with Eq. (19). Right panel: we plot of the difference between the induced metric and the identity matrix for the new autoencoder and the points $\{e_p\}$ where we try to find a Riemann coordinate system.

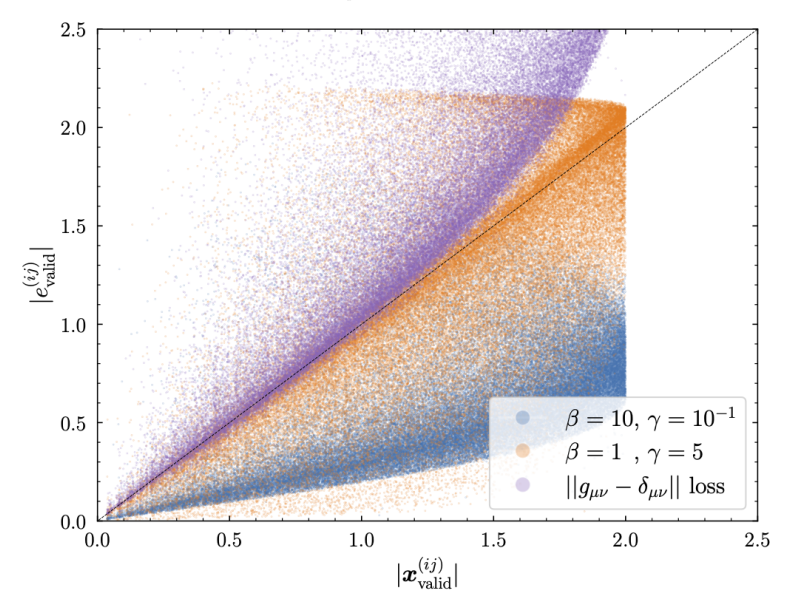


FIG. 11b: Scatter plot of the distances in the embedding space vs. the Euclidean distances in the latent space for 1% of pairs of validation points, for the autoencoder trained with the loss of Eq. (19) in addition to the two autoencoders shown in Fig. 8.

C. "Riemann normal coordinates" autoencoder loss for unit sphere

In this short appendix we show the results of training the same autoencoder of Appendix A with a distance preservation term in the loss different than Eq. (13). More precisely, the loss we use now is

$$L_{\text{distance preservation}} = \frac{1}{n_{\text{train}}} \sum_{p=1}^{n_{\text{train}}} ||g_{\mu\nu}(e_p) - \delta_{\mu\nu}||, \qquad (19)$$

where $e_p = \mathcal{E}(\boldsymbol{x}_p)$ are the latent coordinates of the n_{train} \boldsymbol{x}_p points in the training set that are the closest (with distance within 5×10^{-3}) to the unit cube enclosing the unit sphere.¹¹ Here $||\cdot||$ is the Frobenius norm (not the Frobenius norm squared) and $g_{\mu\nu}$ is the metric of Eq. (11). We also fix $\alpha = 1 = \beta$. The results are shown in Fig. 11a: we see that the autoencoder performs sensibly worse in reconstructing the sphere than those discussed in the main text. It is important to emphasize, though, that we did not try to refine the training of the autoencoder in any way after a first and relatively rough pass.

Fig. 11b is the equivalent of Fig. 8, including also the autoencoder trained with the new loss. While we see that even with this new loss the distances are not preserved as well as for the template banks discussed in Section 2.2, there is a marked improvement over the autoencoders of Appendix A, especially for small distances. It is also interesting that in this case all points seem to lie above the diagonal: while distances are not preserved, the latent-space ones seem to be consistently larger than the embedding-space ones. It would be interesting to investigate this example in more detail, possibly changing Eq. (19) to compute the Frobenius loss squared, or choosing different values for the α/β ratio.

D. "Riemann normal coordinates" autoencoder loss for cylinder

In Appendix B we showed that using the loss of Eq. (13) we cannot find a coordinate system on the cylinder where the metric is flat. Let us then investigate a different loss, similar to Eq. (19). Unlike in Appendix C, we take the x_p points to be all the training points, not just a subset of them (so now we have $n_{\text{train}} = N_{\text{train}}$). We train an autoencoder with the same architecture as in Appendix A with this loss, and show the results in Fig. 12.

Besides the fact that we manage to find a coordinate system where the metric is flat using this loss, another interesting takeaway seems to be that the autoencoder naturally seems to split the cylinder in two "halves", as we see in the right panel of Fig. 12b. What the two halves correspond to in terms of (θ, y) variables is shown in Fig. 13. It would be interesting to investigate if conditional autoencoders (see e.g. https://behavenet.readthedocs.io/en/develop/source/user_guide.conditional_autoencoders.html) could be employed for our GW template banks if we were to encounter the case where the manifold is flat but without boundary, possibly allowing us to keep the simple loss of Eq. (6) and still finding a set of multiple coordinate systems where the metric is close to $\mathcal{N}^2\delta_{\mu\nu}$. We also notice that the reconstruction of $\rho = \sqrt{x^2 + z^2}$ and y is not as good as the autoencoders in Appendix B: this could possibly be improved with a change of architecture and also by not imposing the distance preservation loss at every training point, but only over a subset of them. More precisely, one should batch the training set, and impose the distance preservation loss over a random subset of each batch at every training epoch.¹²

¹¹ Notice that when training with this loss we put all the training data in a single batch.

Notice that all the results for the cylinder presented in this appendix and in Appendices A and B were obtained without batching the training dataset. Regarding the results in the main text, we did not investigate if batching could help with obtaining a better distance preservation than the one shown in Fig. 10b. Given how bad the loss of Eq. (13) fails at finding a coordinate system where $g_{\mu\nu} \approx \delta_{\mu\nu}$, even with varying α/β ratio and γ , we do not expect this would change Fig. 10b much.

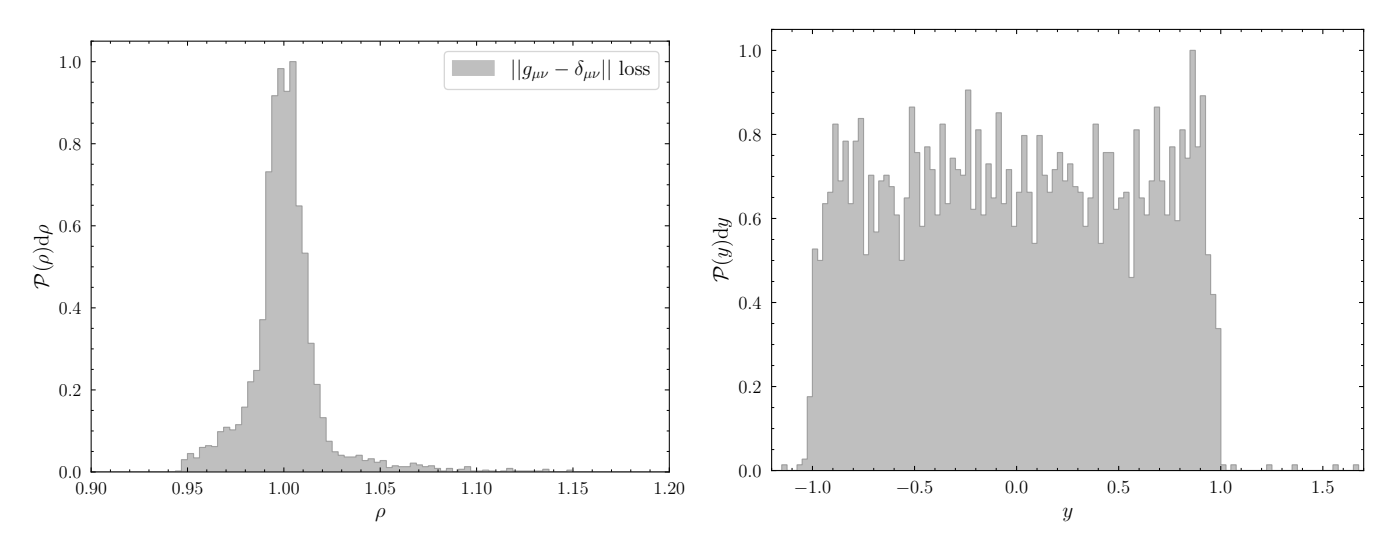


FIG. 12a: Same as in Fig. 10a, but for the autoencoder trained with the loss of Eq. (19) (imposed over all the training set in the case of a flat manifold like the cylinder).

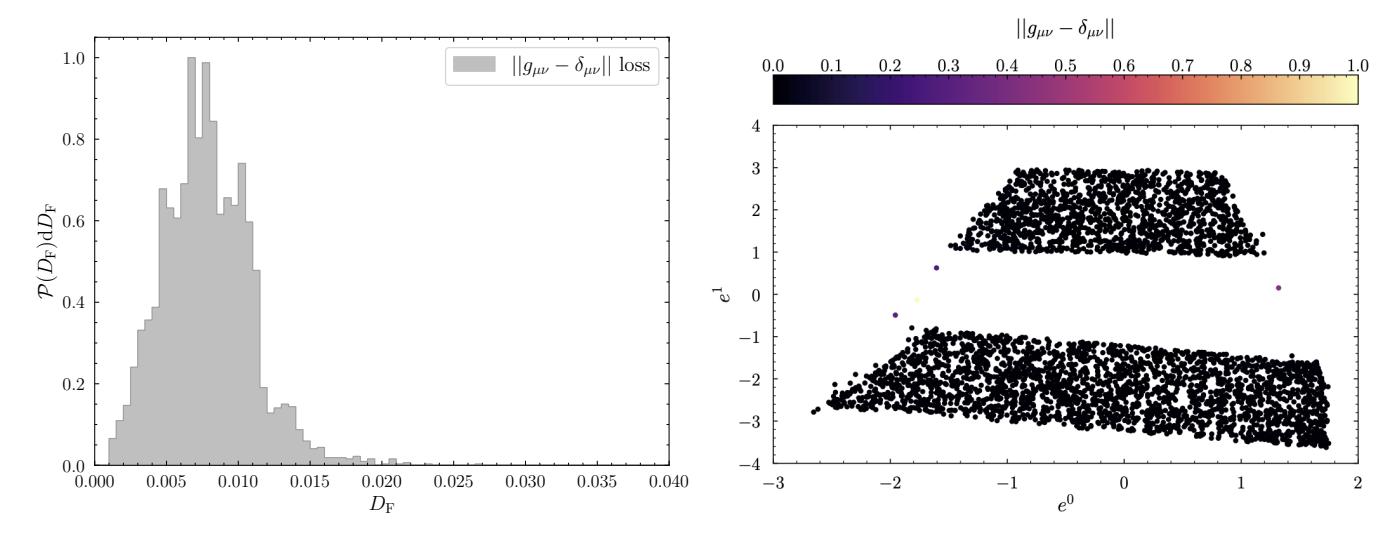


FIG. 12b: The left panel shows the distribution of validation Frobenius distances $||g_{\mu\nu}(e_{\text{valid}}) - \delta_{\mu\nu}|| = D_{\text{F}}$ for the autoencoder of Fig. 12a: only 4 points have $D_{\text{F}} > 0.04$. The right panel shows a scatter plot similar to the right panel of Fig. 11a: we show all validation latent-space points colored by the value of D_{F} , confirming the fact that the loss of Eq. (19) succeeds at finding a coordinate system where the metric is flat.

E. Curvature of GW template banks

In Fig. 14 we see that the bank BBH-5, $\mathcal{M} \in [14.7, 23.9] \, M_{\odot}$ ("Bank 5" hereafter) has a bigger scatter in the distance preservation than the other three banks discussed in the main text. We also checked that this bank is the only one to show this behavior across all banks and sub-banks. We can then compute the curvature of the bank in a similar way as in Appendix A. Since in this case we do not have a target curvature, instead of estimating the Ricci scalar we look at

$$\sqrt{g} R \sim \partial \partial \ln g + (\partial \ln g)^2 . \tag{20}$$

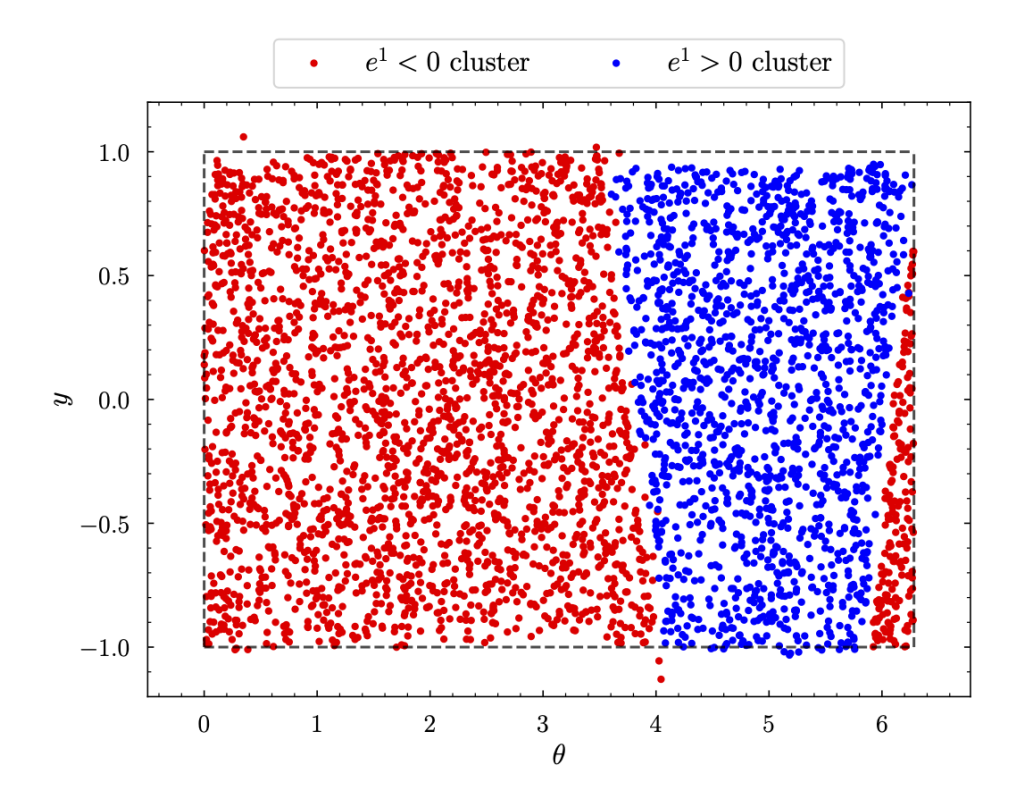


FIG. 13: The two regions in (θ, y) space corresponding to the two clusters shown in the right panel of Fig. 12b. We drop the 4 points with $D_{\rm F} > 0.04$ that – not coincidentally – are the ones that in that figure do not fall in either of the clusters but instead "link" the two clusters.

In this way, we are insensitive to the overall size of the metric in 2 dimensions and we have a fair estimate of the curvature radius (recall that the Riemann tensor is essentially of the form $\partial \partial \ln g + (\partial \ln g)^2$). We proceed in the same way as for the sphere: our estimator for the curvature is

$$\frac{\sqrt{g(e)} R(e)}{2} \approx \frac{\sqrt{g(e)} P_0^1(\partial D_{\epsilon}(e))}{\int_{D_{\epsilon}(e)} d^2 e' g_{00}(e')} , \qquad (21)$$

where again the holonomy is computed around a circle $\partial D_{\epsilon}(e)$ of radius ϵ centered in e.

We choose 12288 physical points for the two banks, making sure that they are at least a distance of 0.05^{13} from the 99.7% CL contour in order to be sure that all the circles around which we compute the holonomy are also inside this contour. We then carry out the same procedure as in Appendix A to compute the numerator and denominator of Eq. (21). The results are shown in Fig. 15: we see that while both banks have a distribution of the curvature consistent with zero, the higher-mass bank has a spread in curvature which is around two orders of magnitude larger than the lower mass bank. This was expected from what we saw in Fig. 14. Also, it is important to emphasize that the curvature is an invariant of the manifold: hence this result is completely independent of the choices of α, β, γ we use when training the autoencoders (as long as both of them describe the respective manifolds with a comparable reconstruction error).

This difference in the spread of curvature notwithstanding, Fig. 16 shows that the effectualness tests for both banks yield comparable results, even if for Bank 5 we see that even after grid refinement a 0.3% fraction of test waveforms has an overlap with their best match in the bank less than 0.95, at variance with Bank 0 for which this fraction is

¹³ Notice that this is intended as Euclidean distance in 2 dimensions, consistently with the formulation of the non-Abelian Stokes theorem.

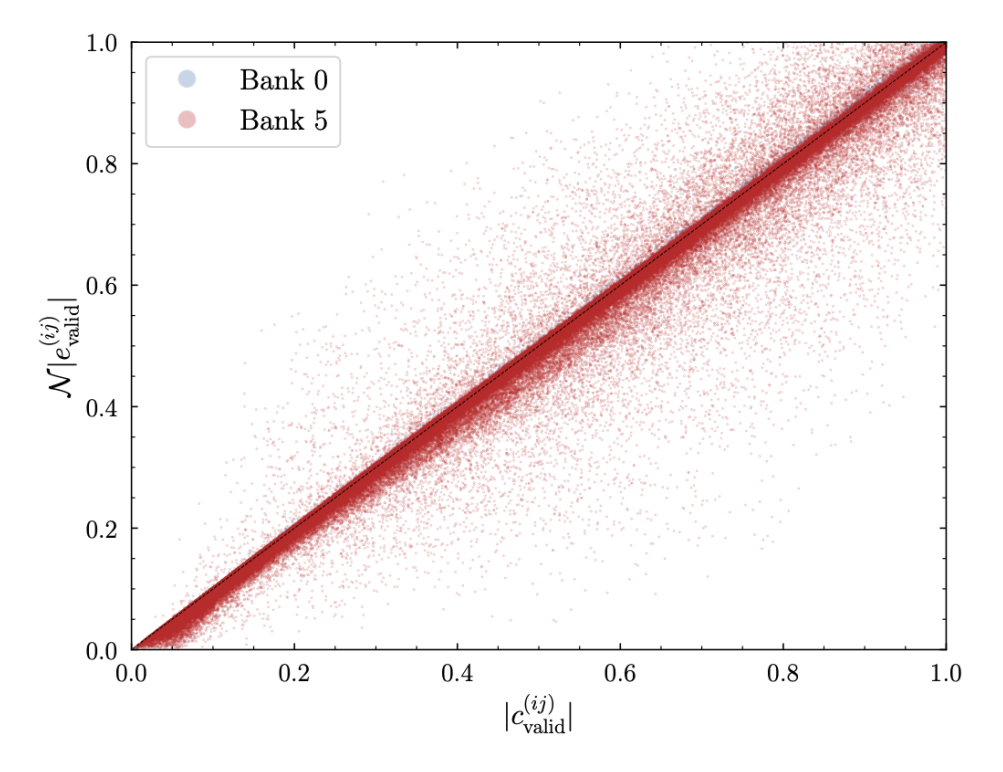


FIG. 14: Same as Fig. 4, but for Bank 0 and the bank BBH-5, $\mathcal{M} \in [14.7, 23.9] \, M_{\odot}$ (Bank 5). At variance with Fig. 4 we plot all pairs of distances such that $|c_{\mathrm{valid}}^{(ij)}| \leq 1$, to emphasize how for Bank 5 distances are not preserved as well as the others.

closer to 0.1%. Finally, we notice that the two normalization factors \mathcal{N} are respectively equal to 55.6 and 3.4 for the two banks: hence in the first case we have a grid size of order $\Delta e = 0.55/\mathcal{N} \approx 10^{-2}$, and in the second case of order $\Delta e = 0.55/\mathcal{N} \approx 10^{-1}$. If we estimate by eye the spread of the inverse of curvature radius of the first bank to be 2×10^{-3} , and 0.5 for the second bank, we see that the grid size is many orders of magnitude smaller than the curvature radius for the lower-mass bank compared to the higher-mass bank. We do not comment more on the relation between grid size and bank curvature in this paper, leaving a more detailed investigation to future work.

F. Autoencoder for COBRA

In Section 3 we discussed the idea of constructing an autoencoder for the SVD decomposition of the linear power spectrum of Ref. [21]. In Fig. 6 we have shown what we could call the decoder in this setup. We just trained a MLP to reproduce the c^A in terms of the cosmological parameters $\theta = (\omega_c, \omega_b, n_s)$, reaching a precision slightly better than the RBF interpolation of [21]. If we want to actually obtain a full autoencoder, we also need to construct and train the encoder, with the constraint that now we want that the latent space is the space of θ^μ . To this purpose, we constructed an encoder with a 16-dimensional input layer, 8 hidden layers each containing 128 neurons and a GELU activation, and a 3-dimensional output layer to go from the d^A , defined as c^A/\mathcal{N} , to the latent space of some variables e^μ . Then, instead of forcing via a simple MSE loss that $e^\mu \approx \theta^\mu$, in order to add flexibility we constructed an invertible transformation f^μ using zuko with the goal that $\theta^\mu = f^\mu(e)$. More precisely, f^μ is a composition of a sequence of 24 Masked Autoregressive Transforms (4 repetitions of 3! = 6 permutations) that utilize Monotonic Affine Transforms as their univariate components. The parameters for the Monotonic Affine Transform are predicted by an internal neural network architecture consisting of 4 hidden layers each with 64 neurons and a GELU activation function. These transforms are followed by the composition with an untrainable sigmoid transform and finally with an affine transformation acting separately on each e^μ in order to bring them inside the box covered by the uniform

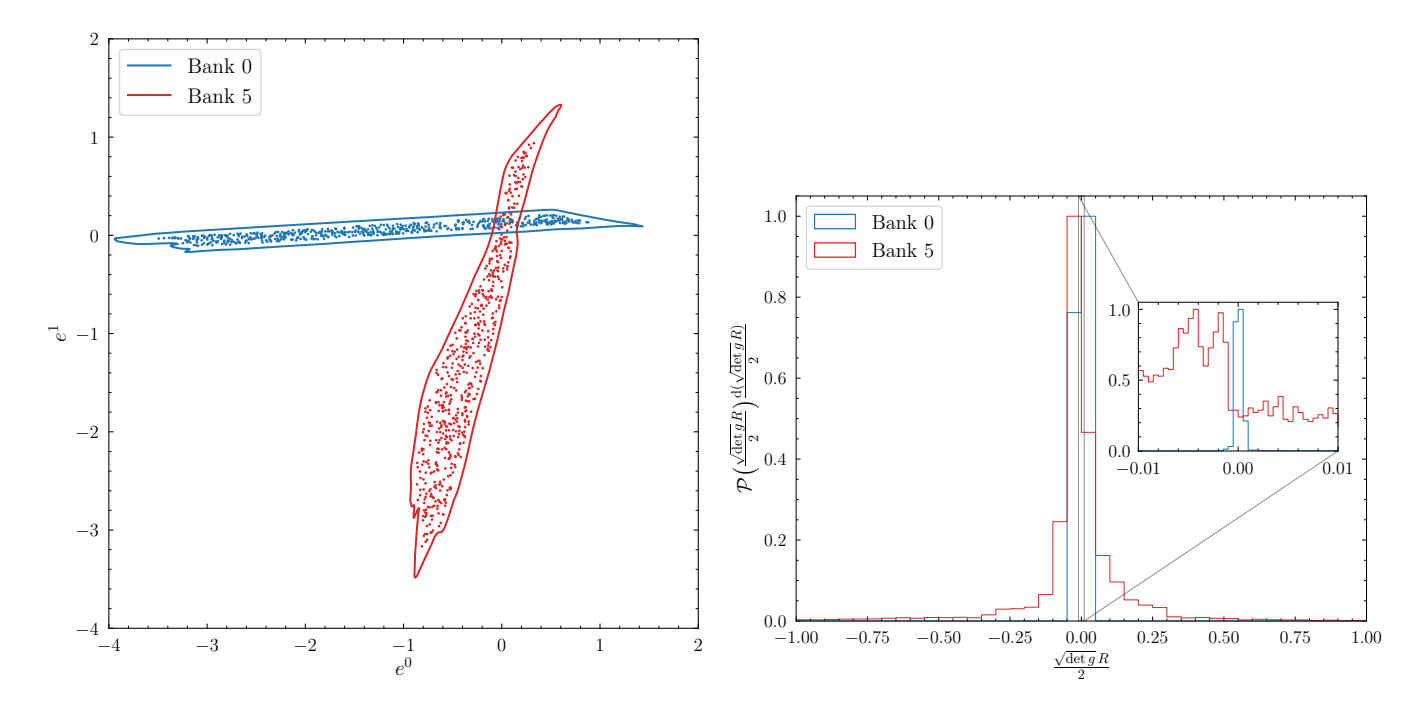


FIG. 15: The left panel shows the 99.7% CL contours of the distribution of the latent-space points (the encoding of the SVD components c^A) for Bank 0 and Bank 5, together with 5% of the 12288 points used to compute the curvature of the banks (notice that in this plot we use the autoencoders and normalizing flows refined to torch.float64 precision). The right panel shows the distribution of $\sqrt{g} R/2$ for the two banks (in the case of Bank 5, we drop 698 points that have estimated $|\sqrt{g} R/2|$ significantly larger than 1 to allow the two histograms to be shown in the same plot).

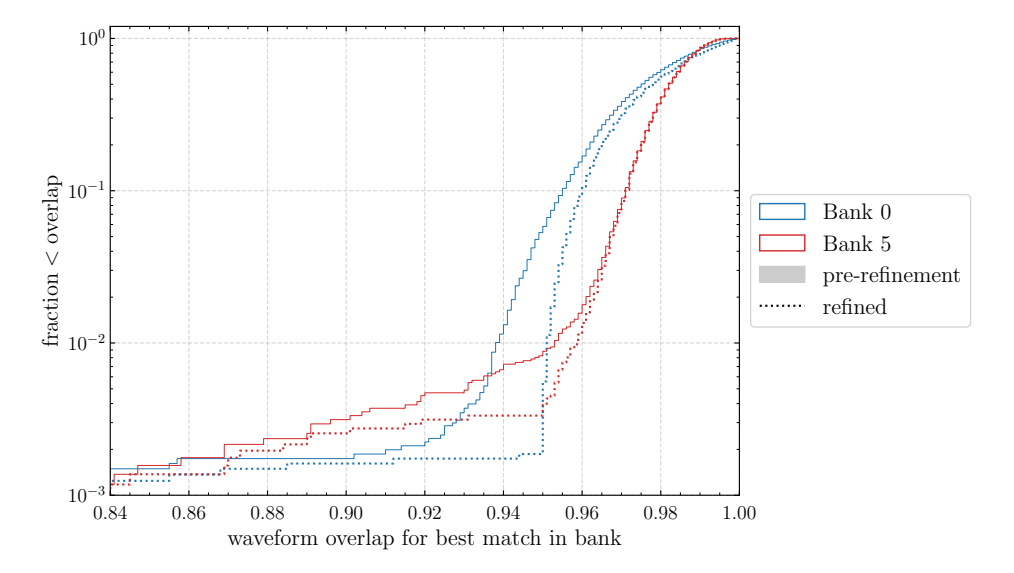


FIG. 16: Effectualness of the template banks for Bank 0 and Bank 5. We see that the higher-mass (and higher-curvature) one benefits from a grid refinement slightly less than the lower-mass one.

and structured grid used in Ref. [21]. In other words, our architecture is

$$c^A \xrightarrow{\mathcal{E}} e^{\mu} \xrightarrow{f} \theta^{\mu} \xrightarrow{\mathcal{D}} c^A$$
 (22)

As a first pass, we train both the "flow" f^{μ} and the autoencoder – the first teacher for a possible transfer learning to improve precision at a later stage – with the loss being a sum of three terms (each with the same overall weight):

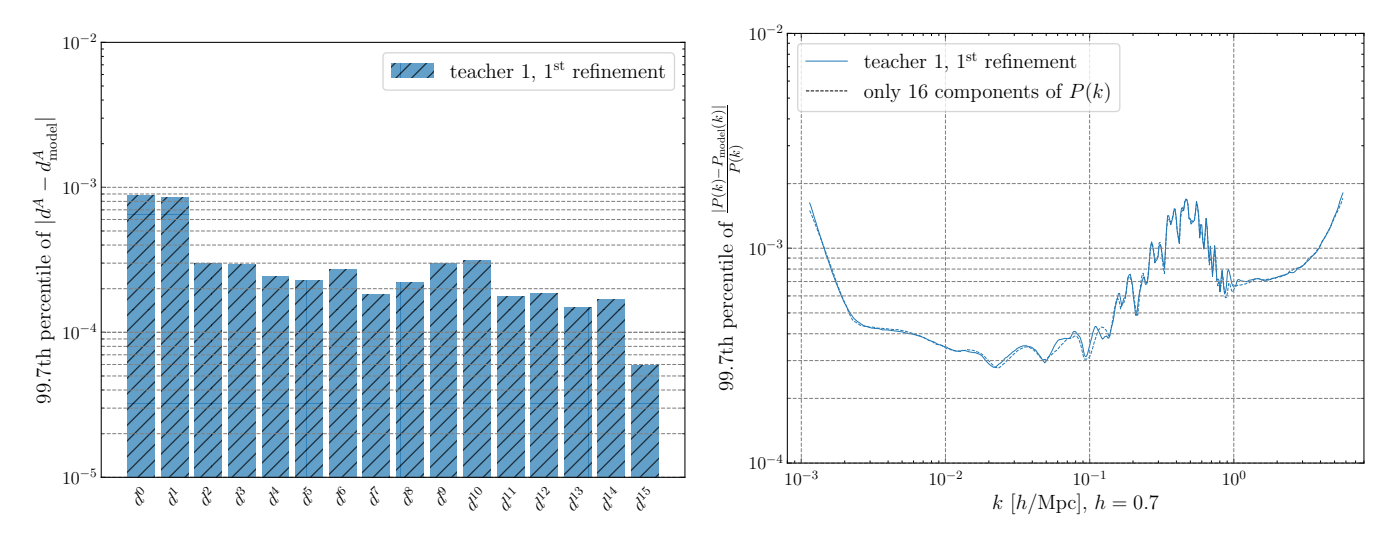


FIG. 17a: Same as Fig. 6, but for the autoencoder architecture presented in Eq. (22). We show only the result of a preliminary pass, that can be considered just as the training of a first "teacher" for a future ensemble + transfer learning procedure, in case that more precision is needed.



FIG. 17b: 99.7th percentile of the relative error in the validation cosmological parameters reconstructed via the $d^A \to e^\mu \to \theta^\mu$ transformation described in Eq. (22). We see that it is ω_b in particular that is difficult to reconstruct.

an MSE loss for $d^A - \tilde{d}_{\text{train}}^A$ (where $\tilde{d}_{\text{train}}^A$ is again defined by $\mathcal{D}^A(\mathcal{E}(d_{\text{train}}))$, like in the training of the autoencoders in the main text), one for $\theta^\mu - f^\mu(e)$, and one for $d^A - \mathcal{D}^A(p)$. The decoder weights are initialized to those of the one shown in orange in Fig. 6. The results of this preliminary first pass are shown in Fig. 17: while it is clear that more refinement is needed in order both reproduce the precision of Fig. 6 in the $\theta^\mu \to d^A \to P(k)$ mapping, and the precision in our recovery of cosmological parameters $P(k) \to d^A \to e^\mu \to \theta^\mu$ is not optimal – especially in the case of ω_b – our architecture is clearly able to find an "inverse" of CAMB in this particular setup where we vary $(\omega_c, \omega_b, n_s)$. Notice also that it is possible our architecture is not the bottleneck in getting from spectra to cosmological parameters, since from the right panel of Fig. 6 we see that the improvement in precision after we refine our decoder does not translate in a similar improvement on the spectra, likely suggesting that we are dominated by the error we are making

when we neglect SVD components beyond A = 15, that seem to be needed to capture the BAO wiggles between 0.1 h/Mpc and 1 h/Mpc to the precision of $\sim 10^{-4}$.

We conclude by pointing out that we were motivated to use the invertible function f^{μ} since in principle, had we trained the autoencoder only with a reconstruction loss forcing $e^{\mu} \approx \theta^{\mu}$, it would have been difficult for it to respect the distribution of cosmological parameters in our training set. It should be possible to enforce the distribution of e^{μ} to be such that the distribution of θ^{μ} is uniform – i.e. to ask $f^{\mu}(e)$ to match also the density of θ^{μ} instead of their position only – by turning on the loss

$$\left\langle -\ln \mathcal{P}_{\theta}(f(e)) \cdot \left| \frac{\partial f(e)}{\partial e} \right| \right\rangle_{e}$$
, (23)

where \mathcal{P}_{θ} is the uniform distribution inside the box used in Ref. [21]. This could be a next step once we move on from a training set consisting of points on a uniform and structured grid (for which the distribution is more akin to a sum of Dirac delta functions). Moreover, having the function f could be useful if later we want to impose the latent space to have some specific property, e.g. distance preservation, or as a starting point for the training of a variational autoencoder to learn the posterior on cosmological parameters.

- D. Wadekar, T. Venumadhav, A. K. Mehta, J. Roulet, S. Olsen, J. Mushkin, B. Zackay, and M. Zaldarriaga, Phys. Rev. D 110, 084035 (2024), arXiv:2310.15233 [gr-qc].
- [2] D. Wadekar, J. Roulet, T. Venumadhav, A. K. Mehta, B. Zackay, J. Mushkin, S. Olsen, and M. Zaldarriaga, Phys. Rev. D 110, 084035 (2024), arXiv:2312.06631 [gr-qc].
- [3] B. P. Abbott et al. (LIGO Scientific, Virgo), Phys. Rev. X 6, 041015 (2016), arXiv:1606.04856 [gr-qc].
- [4] B. P. Abbott et al. (LIGO Scientific, Virgo), Phys. Rev. X 9, 031040 (2019), arXiv:1811.12907 [astro-ph.HE].
- [5] R. Abbott et al. (LIGO Scientific, Virgo), Phys. Rev. X 11, 021053 (2021), arXiv:2010.14527 [gr-qc].
- [6] S. Sachdev et al. (LIGO Scientific, Virgo), Phys. Rev. D 99, 084063 (2019), arXiv:1901.08580 [gr-qc].
- [7] S. A. Usman et al., Class. Quant. Grav. 33, 215004 (2016), arXiv:1508.02357 [gr-qc].
- [8] N. Andres et al., Class. Quant. Grav. 39, 055002 (2022).
- [9] R. Abbott et al. (LIGO Scientific, Virgo, KAGRA), Phys. Rev. X 13, 011048 (2023), arXiv:2111.03606 [gr-qc].
- [10] R. Abbott et al. (LIGO Scientific, Virgo, KAGRA), Phys. Rev. X 14, 031024 (2024), arXiv:2404.04248 [astro-ph.HE].
- [11] T. Venumadhav, B. Zackay, J. Roulet, L. Dai, and M. Zaldarriaga, Phys. Rev. D 101, 083030 (2020), arXiv:1904.07214 [astro-ph.HE].
- [12] S. Olsen et al., Phys. Rev. D 106, 043009 (2022), arXiv:2201.02252 [gr-qc].
- [13] A. K. Mehta et al., Phys. Rev. D 110, 084035 (2024), arXiv:2311.06061 [gr-qc].
- [14] H. S. Chia et al., Phys. Rev. D 108, 104044 (2023), arXiv:2306.00050 [gr-qc].
- [15] A. H. Nitz et al., Astrophys. J. 891, 123 (2020), arXiv:1910.05331 [astro-ph.HE].
- [16] A. H. Nitz et al., Phys. Rev. D 105, 022001 (2022), arXiv:2105.09151 [astro-ph.HE].
- [17] A. H. Nitz et al., Astrophys. J. 946, 59 (2023), arXiv:2112.06878 [astro-ph.HE].
- [18] J. Roulet, L. Dai, T. Venumadhav, B. Zackay, and M. Zaldarriaga, Phys. Rev. D 99, 123022 (2019), arXiv:1904.01683 [astro-ph.IM].
- [19] C. Durkan, A. Bekasov, I. Murray, and G. Papamakarios, "Neural spline flows," (2019), arXiv:1906.04032 [stat.ML].
- [20] S. Schwarz, M. Herrmann, A. Sturm, and M. Wardetzky, Foundations of Computational Mathematics 25, 145–161 (2023).
- [21] T. Bakx, N. E. Chisari, and Z. Vlah, Phys. Rev. Lett. 134, 191002 (2025), arXiv:2407.04660 [astro-ph.CO].
- [22] O. H. E. Philcox, M. M. Ivanov, M. Zaldarriaga, M. Simonovic, and M. Schmittfull, Phys. Rev. D 103, 043508 (2021), arXiv:2009.03311 [astro-ph.CO].
- [23] Á. González, Mathematical Geosciences 42, 49 (2010), arXiv:0912.4540 [math.MG].
- [24] S. M. Carroll, Spacetime and Geometry: An Introduction to General Relativity (Cambridge University Press, 2019).
- [25] B. Broda, (2000), arXiv:math-ph/0012035.